

The SQUALO project (Star formation in QUIescent And Luminous Objects) I: clump-fed accretion mechanism in high-mass star-forming objects

A. Traficante,^{1*} B. M. Jones^{2,3}, A. Avison^{2,4,5}, G. A. Fuller^{2,3,6}, M. Benedettini¹, D. Elia¹, S. Molinari¹, N. Peretto⁷, S. Pezzuto¹, T. Pillai⁸, K. L. J. Rygl⁹ E. Schisano¹ and R. J. Smith²

¹*IAPS-INAF, Via Fosso del Cavaliere, 100, I-00133, Rome, Italy*

²*Jodrell Bank Centre for Astrophysics, Department of Physics and Astronomy, The University of Manchester, Manchester, M13 9PL, UK*

³*I. Physikalisches Institut, Universität zu Köln, Zùlpicher Str.77, D-50937 Köln, Germany*

⁴*UK ALMA Regional Centre Node, M13 9PL, UK*

⁵*SKA Observatory, Jodrell Bank, Lower Withington, Macclesfield, SK11 9FT*

⁶*Intituto de Astrofísica de Andalucia (CSIC), Glorieta de al Astronomia s/n E-18008, Granada, Spain*

⁷*School of Physics and Astronomy, Cardiff University, Queen's Buildings, The Parade, Cardiff, CF243AA, UK*

⁸*Institute for Astrophysical Research, Boston University, 725 Commonwealth Avenue, Boston MA 02215, USA*

⁹*INAF Institute of Radio Astronomy, Bologna, Italy*

Accepted XXX. Received YYY; in original form ZZZ

ABSTRACT

The formation mechanism of the most massive stars is far from completely understood. It is still unclear if the formation is core-fed or clump-fed, i.e. if the process is an extension of what happens in low-mass stars, or if the process is more dynamical such as a continuous, multi-scale accretion from the gas at parsec (or even larger) scales. In this context we introduce the SQUALO project, an ALMA 1.3 mm and 3 mm survey designed to investigate the properties of 13 massive clumps selected at various evolutionary stages, with the common feature that they all show evidence for accretion at the clump scale. In this work we present the results obtained from the 1.3 mm continuum data. Our observations identify 55 objects with masses in the range $0.4 \leq M \leq 309 M_{\odot}$, with evidence that the youngest clumps already present some degree of fragmentation. The data show that physical properties such as mass and surface density of the fragments and their parent clumps are tightly correlated. The minimum distance between fragments decreases with evolution, suggesting a dynamical scenario in which massive clumps first fragment under the influence of non-thermal motions driven by the competition between turbulence and gravity. With time gravitational collapse takes over and the fragments organize themselves into more thermally supported objects while continuing to accrete from their parent clump. Finally, one source does not fragment, suggesting that the support of other mechanisms (such as magnetic fields) is crucial only in specific star-forming regions.

Key words: ISM: kinematics and dynamics – Interstellar Medium (ISM), Nebulae, stars: formation – Stars, radio continuum: ISM – Resolved and unresolved sources as a function of wavelength, Galaxy: kinematics and dynamics – The Galaxy

1 INTRODUCTION

The formation of the most massive stars ($M > 8 M_{\odot}$) remains still a highly debated question. A critical aspect to understand is the mechanism that feeds the massive stars from their surroundings. The so-called *core-fed* scenario suggests that the stars gather their mass from their parent core (McKee & Tan 2003; Tan et al. 2014), relatively pressure-confined from its natal clump, in a similar fashion to the low-mass star formation mechanism (Shu 1977). In this sce-

nario the pre-stellar cores must be quite massive: accounting for a star-formation efficiency of $\simeq 40\%$ from cores to stars (Könyves et al. 2015, 2020), to form a $\simeq 10 M_{\odot}$ star we must observe at least a $\simeq 25 M_{\odot}$ pre-stellar core. The hunt for such high-mass pre-stellar cores has been carried out for years now (Motte et al. 2018), but the results are inconclusive. Studies based on the analysis of far-infrared (FIR)/sub-mm Galactic Plane surveys suggest that massive pre-stellar cores are extremely rare, if ever observed (Ginsburg et al. 2012; Traficante et al. 2018a). Moreover, studies of clump fragmentation at sub-parsec scales, which are significantly increasing in the ALMA era, show that massive, pre-stellar

* E-mail: alessio.traficante@inaf.it

objects with no hint of ongoing star-formation activity do not seem to exist at all (Svoboda et al. 2019; Sanhueza et al. 2019), except for a handful of very isolated cases (Nony et al. 2018). This massive pre-stellar phase must be extremely fast, and therefore very rare to identify (Ginsburg et al. 2012).

Alternatively, massive pre-stellar cores may not exist at all: the formation of massive stars may be a much more dynamical process, small seeds compete to accrete and form massive protostellar objects (Bonnell & Bate 2006) and they are themselves fed by gas in the parent clump. This is a hierarchical process which forms dynamically connected structures at various scales from the parsec, clump scales (or even larger) down to the formation of the single cores in a global collapse, *clump-fed* scenario (Smith et al. 2009; Wang et al. 2010; Peretto et al. 2013; Vázquez-Semadeni et al. 2019; Peretto et al. 2020). This interpretation would explain why in some sub-parsec resolutions surveys of massive clumps we found resolved fragments at different scales, from 0.06 pc (Csengeri et al. 2017) down to 1000-2000 AU scales (Beuther et al. 2018; Sanhueza et al. 2019; Svoboda et al. 2019). And this model is corroborated by a large number of single-dish observations of clumps at various evolutionary stages that show high accretion rates of the order of $\dot{M} \simeq 10^{-3} - 10^{-4} M_{\odot} \text{ yr}^{-1}$ (Fuller et al. 2005; Rygl et al. 2010; He et al. 2015; Wyrowski et al. 2016; Traficante et al. 2018a).

A direct link from accretion at clump scales and the formation of fragments at sub-parsec scales within each star-forming clumps, however, has still not yet been identified. There are examples in the literature of regions that show accretion at core scales (Yuan et al. 2018; Cortes et al. 2019; Neupane et al. 2020), which sometimes have simultaneous accretion at the clump scales, with further evidence of global collapse of the parent filaments (Peretto et al. 2013; Yuan et al. 2018). However, this large-scale accretion may not necessarily be responsible for the observed small-scale accretion, which could remain relatively distinct from the parsec-scales dynamics (Henshaw et al. 2014).

In this paper we discuss the first results from the SQUALO (Star formation in QUIescent And Luminous Objects) survey. SQUALO is an ALMA project approved in Cycle 6 (project ID 2018.1.00443.S) whose main goal is to investigate the connection between clump scales and core scales properties at various evolutionary phases for massive objects that show clear signatures of gas accretion at the parsec scale. We present in particular the ALMA sample of the 13 clumps selected in the project and the results obtained from the ALMA observations in the continuum at 1.3mm. These new ALMA data are used to investigate the fragmentation properties of the clumps, and to correlate them with the properties of the parent clumps, presenting a first attempt to connect parsec and sub-parsec scales on a sample of objects that are undergoing clump-scales accretion at various evolutionary stages. A detailed study of the accretion properties using ALMA Band 3 data will be the subject of a forthcoming SQUALO paper (Paper II, Traficante et al. *in prep.*).

The work is divided as follows: in Section 2 we present the sample selection, based on the catalogue of Hi-GAL clumps analyzed in Traficante et al. (2017) and Traficante et al. (2018b), and the new SQUALO observations; in Section 3 we describe how we have analyzed the clumps data and we detail how we have extracted the main properties of the fragments

in each clump; in Section 4 we present the results derived from the analysis of the ALMA data alone, while in Section 5 we correlate the clumps properties with those of their inner fragments. Here we show how the fragment and the clump properties are intimately connected. Finally, in Section 6 we summarize our results and draw our conclusions.

2 SOURCES SELECTION AND OBSERVATIONS

We started the sample selection from the massive clumps analyzed in Traficante et al. (2018b), who combined the Hi-GAL clumps identified in the inner Galaxy by Elia et al. (2017) with the sample of 3 mm molecular line transitions observed with the MALT90 survey (Jackson et al. 2013). The Elia et al. (2017) catalogue contains more than 100000 clumps identified in the Galactic plane with the Hi-GAL survey (Molinari et al. 2010) in the longitude range $-71^{\circ} \leq l \leq 67^{\circ}$ with well defined spectral energy distributions (SEDs), i.e. with at least three consecutive photometric points among the 5 available within the Hi-GAL survey ($70 \mu\text{m}$, $160 \mu\text{m}$, $250 \mu\text{m}$, $350 \mu\text{m}$ and $500 \mu\text{m}$). The MALT90 survey mapped 16 molecular lines in the 3mm band with the MOPRA telescope in a $3.4' \times 3.4'$ region for 2012 clumps in the longitude range $3^{\circ} \leq l \leq 20^{\circ}$ in the first quadrant and $-60^{\circ} \leq l \leq -3^{\circ}$ in the fourth quadrant, selected from the ATLASGAL survey (Schuller et al. 2009). The spatial resolution is $38''$, the spectral resolution of 0.11 km s^{-1} and the typical system temperature is $180 \leq T_{\text{sys}} \leq 300\text{K}$, for a typical *r.m.s.* noise of 250 mK per channel (Jackson et al. 2013).

Traficante et al. (2018b) combined these two catalogues and identified 213 clumps with well defined dust properties and gas kinematics, determined from their N_2H^+ (1–0) spectra, among which 21 showed blue-asymmetric spectra in their HCO^+ (1–0) line profiles interpreted as evidence of parsec-scale infall motions (Fuller et al. 2005).

For the SQUALO project we extracted a sub-sample of 10 massive clumps with these infall profiles and with the following properties: mass $M \geq 170 M_{\odot}$, surface density $\Sigma \geq 1 \text{ g cm}^{-2}$ (a good indicator that clumps may form high-mass stars, e.g. Tan et al. 2014), at a distance $d \leq 5.5 \text{ kpc}$ and relatively isolated from other clumps after visual inspection of the Hi-GAL column density maps.

These 10 clumps cover a luminosity to mass ratio (L/M) range of $4 \leq L/M \leq 107 L_{\odot}/M_{\odot}$. Assuming L/M as evolutionary indicator (Molinari et al. 2008; Molinari et al. 2016b), this initial sample missed the youngest objects ($L/M < 1$, e.g. Molinari et al. 2016b), often observed in absorption or with very weak emission in the Herschel $70 \mu\text{m}$ maps and therefore defined as $70 \mu\text{m}$ -quiet clumps. We then added three sources from the survey of massive $70 \mu\text{m}$ -quiet clumps of Traficante et al. (2017) following the same selection criteria of the more evolved sources, including that these 3 clumps also show blue-asymmetric HCO^+ (1–0) line profiles. The kinematics of the gas in these objects have been observed with the IRAM 30m telescope at a spatial resolution of $27''$ and a variable spectral resolution of 0.06 km s^{-1} for the N_2H^+ (1–0) and of $\simeq 0.2 \text{ km s}^{-1}$ for the HCO^+ (1–0) with a typical *r.m.s.* noise per channel of 130–320 mK.

The final SQUALO sample contains 13 sources with a L/M range $0.1 \leq L/M \leq 107 L_{\odot}/M_{\odot}$, with sources classified from

70 μm -quiet up to HII regions, all of them that will likely form high-mass stars and that exhibit parsec-scales infall motions with accretion rates \dot{M} in the range $0.7 \leq \dot{M} \leq 27.3 \times 10^{-3} M_{\odot} \text{ yr}^{-1}$ at the clump scales.

2.1 ALMA observations

2.2 Data calibration

The single-pointings observations for ALMA project 2018.1.00443.S were conducted from 05 October 2018 to 11 January 2019 with two tunings, in bands 3 and 6 respectively. The band 6 science goal was observed as 3 observing blocks on the 12m array, 16 observing blocks on the 7m array and 28 observations with the ALMA Total Power (hereafter TP) dishes. The band 3 data were taken as 7 blocks on the 12m array and 20 blocks on the 7m array. For continuum imaging, only the interferometric data is used.

The band 3 and band 6 tunings were set to have 4 spectral windows (SPWs) that have been further split to optimize the analysis of the continuum and to trace specific lines with high spectral resolution. The central frequency, channel width and total bandwidth of the observed SPWs is given in Table 1. The name of each SPW denotes the key purpose, although other notable lines such as the $J = 1 - 0$ transitions of ^{12}CO and ^{13}CO , are also included in the wide bandwidth band 6 ‘continuum’ windows.

After the observations were complete, the data were downloaded from the ALMA Archive and calibrated using the ALMA pipeline scripts provided by the archive using CASA version 5.4 (McMullin et al. 2007). This resulted in fully calibrated measurement sets for the 12m and 7m arrays. Beyond the ALMA pipeline calibration, further processing and imaging was undertaken in CASA version 5.6 and is described below.

2.3 Interferometric data preparation

In addition to slight differences in tuning between the observation dates, the 7m and 12m correlators output a different bandwidth, with excess in the 7m observations. The spectral windows were first matched into groups corresponding to the same target frequency over all dates, before separating the data set to contain only matching windows and a single array using CASA’s task `split`. Regridding is performed with `mstransform` on each to transform the channels to equally spaced in LSRK (Kinematic Local Standard of Rest) velocity, with the reference frequency set equal to the rest frequency of the target spectral line, or the centre of the window for continuum spectral windows.

The overlap between the 7m and 12m windows is calculated by plotting all data with `plotms` and outputting the spectral axis for each array to a text file. The maximum lower limit and the minimum upper limit of the spectral axes were used to define the common channels in all observations of the source. Each of the data sets were then trimmed to the common spectral range using a further `split` and recombined into a single data set taken with a heterogeneous array for each spectral window.

2.4 Identification of line-free channels

To successfully create continuum images, the channels without lines must first be identified for each spectral window. For the majority of sources in the sample, line identification can be done visually using `plotms` to inspect the amplitude against velocity averaged over all observations. For some sources, human inspection is neither an efficient nor accurate method for identifying continuum channels. The automated line identification algorithm LumberJack is instead used to identify the continuum channels¹. LumberJack utilises a sigma clip and ‘gradient’ analysis (and cross matches the results) of spectral channel flux density values extracted at the location of identified sources to determine regions spectral line free channel regions within the data on a spectral window by spectral window basis. A buffer of 5 channels is also added on either side of detected spectral line regions to ensure that all line emission is removed. See Avison et al. (MNRAS, *submitted*) for further details.

2.5 Joint deconvolution imaging

The image size and pixel size are determined by the combined properties of the interferometric configurations. All imaging is completed in ‘mosaic’ mode to ensure the variable primary beam with baseline is accounted for, necessary for heterogeneous arrays. The field of view is given by the combined primary beam weighted by number of baselines, and the field is imaged to the 20% power level. The image size is set to twice the field of view as mosaic mode requires excess padding to ensure the edges are treated correctly. The pixel size used is $0.2''$ and samples the major axis of the beam with $\simeq 6$ pixels for the band 6 data.

Briggs’ weighting with a robust parameter of 0.5 is used, as recommended by ALMA for combined array imaging. Multi-scale `tclean` was used for all imaging, with the scales to image set to 0 (point source), the size of the synthesised beam and three times the beam size. Cleaning and masking was performed interactively with the task `tclean`. All line-free channels from all spectral windows are combined for maximum sensitivity to create the aggregate bandwidth continuum images used in this paper. In the following, we will consider for the scientific analysis the primary beam (PB) corrected images produced with the described pipeline.

The synthesised beam, linear resolution and achieved *r.m.s.* of each source are given in Table 2. Our data allow us to trace sub-pc fragments of sizes down to $\simeq 0.01$ pc ($\simeq 2130$ AU) in the closest objects, and down to $\simeq 0.04$ pc ($\simeq 7700$ AU) in the furthest clumps, smaller than the expected core size (0.1 pc, e.g. Di Francesco et al. 2001). The *r.m.s.* varies significantly across the sample (from $\simeq 0.8$ mJy/beam to $\simeq 15.2$ mJy/beam), and it increases in sources with very bright fragments, where due to the limited dynamical range of the maps the local *r.m.s.* is higher than the nominal one.

3 CLUMPS AND FRAGMENTS ANALYSIS

In this Section we describe how we extract the physical and kinematic properties of the clumps and the inner fragments

¹ LumberJack available at <https://github.com/adam-avison/LumberJack>

Band	Name	Central freq. (GHz)	Bandwidth (MHz)	Channel width (MHz)
3	Continuum	87.800	1875.0	1.129
	HCO ⁺ 1-0	89.189	117.19	0.071
	H ¹³ CO ⁺ 1-0	86.754	58.59	0.071
	SiO <i>v</i> =1 2-1	86.243	58.59	0.071
	HCN 1-0	88.631	117.19	0.071
6	Continuum 1	231.100	1875.0	1.129
	Continuum 2	234.000	1875.0	1.129
	CH ₃ CN 12 ₀ -11 ₀ , F=12-11	220.5300	468.75	0.282
	OCS 18-17	218.903	58.59	0.141
	H ₂ CO 3 ₂₁ -2 ₂₀	218.760	58.59	0.141
	H ₂ CO 3 ₂₂ -2 ₂₁	218.476	58.59	0.141
	H ₂ CO 3 ₀₃ -2 ₀₂	218.222	58.59	0.141

Table 1. Spectral tuning for the SQUALO observations made with ALMA. Unless otherwise specified, all targeted transitions are the *v*=0 states.

DESIGNATION	B_{min} (")	B_{maj} (")	B_{PA} (°)	Linear Res. (AU)	<i>r.m.s.</i> (mJy beam ⁻¹)
HIGALBM327.3918+0.1996	1.10	1.25	-54.5	6050	2.68
HIGALBM327.4022+0.4449	1.10	1.25	-54.9	5423	8.67
HIGALBM331.1314-0.2438	1.08	1.26	-64.7	5752	11.53
HIGALBM332.6045-0.1674	1.07	1.27	-67.8	3579	1.15
HIGALBM338.9260+0.6340	1.03	1.12	77.6	4475	3.26
HIGALBM341.2149-0.2359	1.03	1.11	80.3	3683	1.87
HIGALBM343.5212-0.5172	1.02	1.11	85.8	3223	1.07
HIGALBM343.7560-0.1629	1.02	1.11	86.3	2126	15.18
HIGALBM344.1032-0.6609	1.02	1.11	86.7	2128	1.64
HIGALBM344.2210-0.5932	1.02	1.11	87.3	2130	3.81
HIGALBM24.0116+0.4897	1.23	1.46	-88.9	6988	1.42
HIGALBM28.1957-0.0724	1.30	1.49	-87.7	7460	0.78
HIGALBM31.9462+0.0759	1.32	1.49	89.9	7715	0.83

Table 2. *Col. 1*: Source designation ID from the [Elia et al. \(2021\)](#) catalogue; *Cols. 2-4*: Synthesized beam properties (beam minor axis, beam major axis and position angle, respectively) for each of the 13 SQUALO sources. *Col 5*: linear resolution of the average synthesized beam assuming the source distance showed in [Table 3](#); *Col 6*: achieved *r.m.s.* in each map.

from the ancillary catalogues and the new ALMA data. In the hierarchical process of star-formation, the structures we detect could represent some intermediate step between clumps and the innermost cores (the mass concentrations currently forming protostars), and this is the reason why we refer to them with the generic term "fragments".

3.1 Clump analysis

The physical properties of the 13 clumps have been re-evaluated according to the most recent version of the Hi-GAL clumps catalogue ([Elia et al. 2021](#)) in order to produce a coherent sample of parameters. All these clumps have been identified in the Hi-GAL catalogue and all but one, HIGALBM31.9462+0.0759, have a distance assigned based on the [Mège et al. \(2021\)](#) Hi-GAL distances catalogue. In the work of [Elia et al. \(2021\)](#) the physical properties of all the sources with unknown distance have been evaluated assuming a reference value of 1 kpc ([Elia et al. 2021](#)). In our case, HIGALBM31.9462+0.0759 is part of a well known infrared dark cloud complex located at a distance of 5.5 kpc ([Battersby et al. 2014](#)). Therefore, for this source we re-

scaled the [Elia et al. \(2021\)](#) distance-dependent properties to this value. The kinematics of the gas have been taken from [Traficante et al. \(2018b\)](#) and [Traficante et al. \(2017\)](#) for the ten MALT90 sources and the three 70 μ m-quiet clumps respectively. The main properties of the 13 clumps considered for this work are summarized in [Table 3](#).

3.2 Fragment analysis

The first step to determine the physical properties of our objects is to detect the fragments in each ALMA dust continuum image and extract their photometry. There are many possible approaches to extract the photometry from continuum images, so we initially decided to proceed with an "agnostic" approach and perform the photometry using two different algorithms, *Astrodendro* and *Hyper*. In the following, we will consider the results obtained with the *Hyper* code ([Traficante et al. 2015b](#)). We chose this code because it has been specifically designed to: 1) deal with highly variable backgrounds, which is often the case of some of these objects that are embedded in elongated structures, and 2) deblend coupled sources, a situation that we have encountered in our

DESIGNATION	M_{cl} (M_{\odot})	L_{cl} (L_{\odot})	L_{cl}/M_{cl} ($L_{\odot} M_{\odot}^{-1}$)	Σ_{cl} (g cm^{-2})	\dot{M}_{cl} ($10^{-3} M_{\odot} \text{ yr}^{-1}$)	R_{cl} (pc)	T_{cl} (K)	$\alpha_{vir,cl}$	α ($^{\circ}$)	δ ($^{\circ}$)
HIGALBM327.3918+0.1996	1121	14146	12.6	3.82	4.67	0.14	22.9	0.3	15:50:18.646	-53:57:03.254
HIGALBM327.4022+0.4449	2157	73841	34.2	5.57	27.29	0.16	29.6	0.24	15:49:19.454	-53:45:13.190
HIGALBM331.1314-0.2438	2467	54845	22.2	8.99	11.78	0.14	31.3	0.26	16:10:59.686	-51:50:23.104
HIGALBM332.6045-0.1674	177	1405	7.9	2.42	1.63	0.07	19.6	0.73	16:17:29.486	-50:46:09.646
HIGALBM338.9260+0.6340	2689	10280	3.8	4.93	62.1	0.19	19.3	0.23	16:40:13.786	-45:38:28.313
HIGALBM341.2149-0.2359	700	7210	10.3	1.37	2.32	0.18	21.2	0.37	16:52:23.515	-44:27:54.338
HIGALBM343.5212-0.5172	347	7039	20.3	2.37	3.51	0.10	21.3	0.52	17:01:33.986	-42:50:18.98
HIGALBM343.7560-0.1629	461	6778	14.7	4.41	3.83	0.09	23.8	0.32	17:00:49.831	-42:26:09.665
HIGALBM344.1032-0.6609	230	3586	15.6	1.84	8.86	0.09	21.5	1.22	17:04:06.982	-42:27:56.441
HIGALBM344.2210-0.5932	202	21645	107.0	1.88	1.75	0.09	34.1	0.86	17:04:12.830	-42:19:51.704
HIGALBM24.0116+0.4897	1334	158	0.1	1.93	4.0	0.21	10.7	0.16	18:33:18.535	-7:42:23.857
HIGALBM28.1957-0.0724	1598	594	0.4	0.97	0.74	0.33	12.8	0.27	18:43:02.561	-4:14:50.150
HIGALBM31.9462+0.0759	1392	133	0.1	2.5	8.21	0.19	10.3	0.23	18:49:22.207	-0:50:33.536

Table 3. Physical properties of the 13 Hi-GAL clumps selected in the SQUALO survey. These properties have been extracted from the latest release of the Hi-GAL clump catalogue [Elia et al. \(2021\)](#). The physical properties of HIGALBM31.9462+0.0759 have been re-scaled from the Hi-GAL catalogue assuming a distance of 5.5 kpc ([Battersby et al. 2014](#)). *Col.1*: Source designation ID; *Cols.2-3*: mass M_{cl} and luminosity L_{cl} of our sources; *Col.4*: L_{cl}/M_{cl} of the clump, used as evolutionary indicator; *Col. 5*: surface density Σ_{cl} of the clumps; *Col. 6*: mass accretion rate derived from HCO⁺ (1 – 0) or HNC (1 – 0) blue-asymmetric spectra; *Col. 7*: deconvolved radius of the clumps, evaluated from the 2d-Gaussian fit to each source done at 250 μm ([Elia et al. 2021](#)); *Col. 8*: temperature of the clumps; *Col. 9*: virial parameter of the clumps; *Cols. 10-11*: source peak identified in the 160 μm Hi-GAL map; *Col.12*: adopted source distance.

sample (see Figure 1). A detailed comparisons of the different outputs of the two codes are described in Appendix A.

We have tested several thresholds for the source identification with *Hyper* and, after visual inspection of all the different runs, we decided to identify the fragments considering as real objects all the compact sources with peaks above 3 times the *r.m.s.* of each cleaned, PB corrected image, estimated with a sigma-clipping procedure. Here we consider compact sources all objects with maximum aspect ratio equal to 1.5 and with FWHMs not larger than 2 times the beam size. With these identification criteria we found a total of 60 fragments distributed in our 13 clumps. After further inspection we identified 5 fragments, the faintest of the sample, that were located at the edges of the primary beam corrected images (and/or significantly away from the Hi-GAL 250 μm clump footprint), for which the integrated fluxes could not be accurately recovered by *Hyper*. We considered these objects as spurious identifications and removed them from our final selection. In Figures 1 and 2 we show the 13 ALMA images with the 55 fragments included in the final selection (in blue crosses) and the 5 fragments excluded from the analysis (in magenta crosses). In each image are also shown the Hi-GAL 160 μm and 250 μm footprints obtained by the *Cutex* 2d-Gaussian fitting (the green-dotted ellipses). Out of these 55 fragments, 44 are observed within the 160 μm footprint (the shortest Hi-GAL wavelength in common to all our sources). Of the remaining 11 fragments, 7 are within the 250 μm footprint and 4 lie just at the edges of the clump as observed at 250 μm . Although the majority of the fragment formation occurs within the inner regions of the clump traced by the 160 μm emission, $\simeq 20\%$ of objects are associated with the cold outskirts of the clump, traced by the 250 μm (and longer wavelengths) emission.

3.2.1 Radius and mass of the fragments

The FWHMs estimated with the *Hyper* 2D-Gaussian fitting are used to define the major and minor semi-axes of the ellipses across which we perform the aperture photometry of each fragment. The geometrical mean of the two FWHMs is used to estimate the radius of the fragments R_f , which spans the range $0.013 \leq R_f \leq 0.049$ pc. The majority of our fragments are not point-like, but rather moderately resolved structures (Figure 1) but it is possible that some of the objects that we have identified will further fragment into smaller pieces, as observed in higher resolution observations (e.g. [Beuther et al. 2018](#); [Pouteau et al. 2022](#)).

The integrated 1.3 mm flux of each fragment has been converted into mass following the formula (e.g. [Svoboda et al. 2019](#); [Zhang et al. 2020](#)):

$$M_f = \frac{D^2 S_{1.3}}{B_{1.3}(T_f)\kappa_{1.3}} \quad (1)$$

where D is the clump distance, $S_{1.3}$ the integrated flux at 1.3 mm, and $\kappa_{1.3}$ the dust absorption coefficient at 1.3 mm, fixed to $\kappa_{1.3} = 0.005 \text{ cm}^2 \text{ g}^{-1}$ ([Preibisch et al. 1993](#)) that also includes gas-to-dust mass ratio of 100, and T_f , the dust temperature of the dust envelopes of each fragment, which is a key parameter of this formula. Ideally, it should be measured from line emissions that are not strongly affected by outflows or feedback, such as NH₃ (e.g. [Palau et al. 2015](#)), which are not available for our sample. There are other lines in our spectral setup that may be used as temperature tracers, such as H₂CO or CH₃OH. All these lines, however, have been shown to also trace the hot gas around each object associated with outflows and shocks ([Zhang et al. \(2015\)](#)), not just the cold dust envelopes, and they could likely over-estimate the fragment temperatures.

Instead, to infer the temperature of the dust envelopes of the fragments we started from the clump properties, similar to what has been done in recent ALMA works ([Csengeri et al.](#)

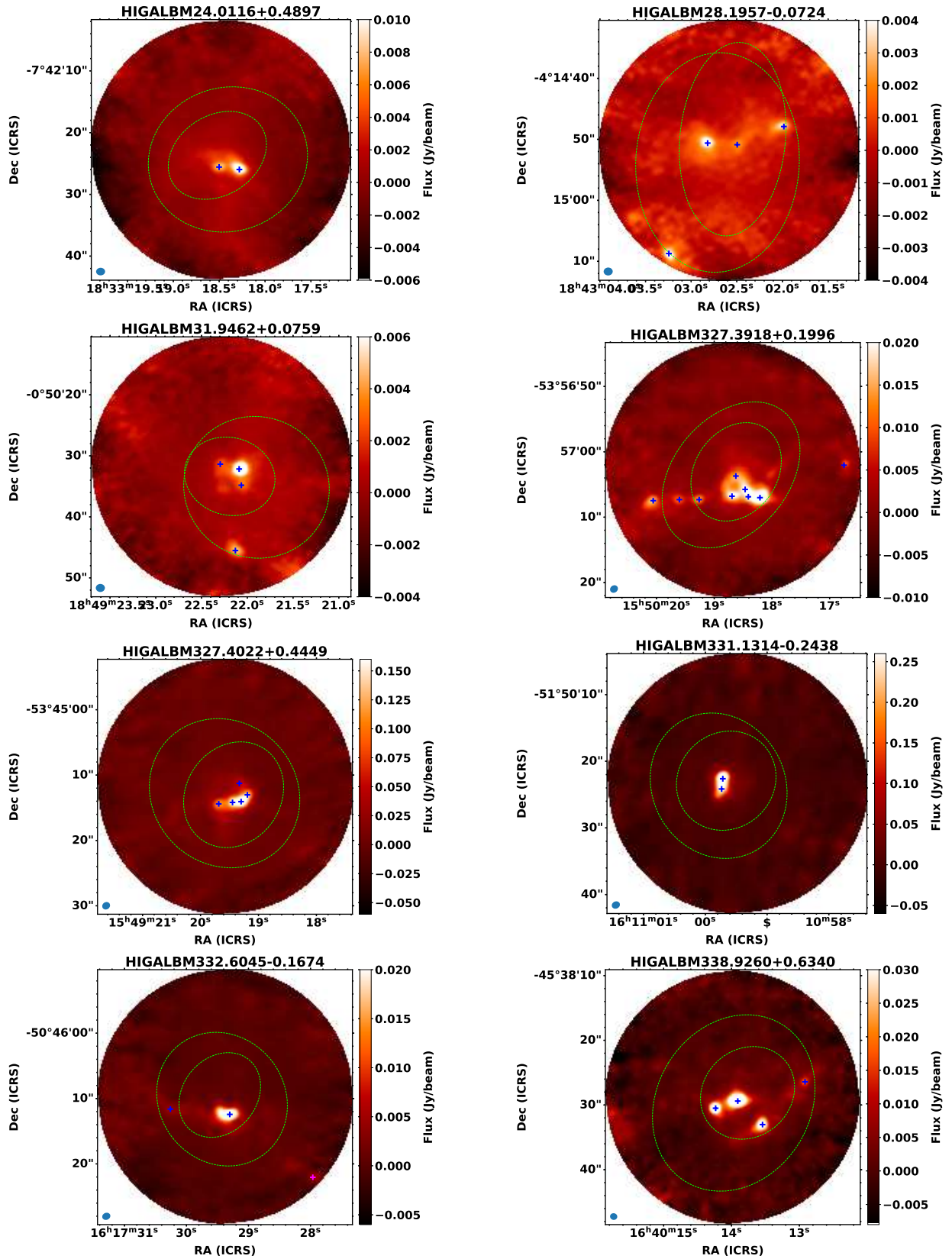


Figure 1. ALMA 1.3 continuum images of the 13 clumps observed in the SQUALO survey. The green ellipses are the Hi-GAL $160\ \mu\text{m}$ and $250\ \mu\text{m}$ footprints. The blue crosses are the centroids of the 55 *Hyper* fragments considered in the scientific analysis, and the magenta crosses are the 5 fragments excluded from the analysis. Sources HIGALBM344.1032-0.6609 and HIGALBM344.2210-0.5932 had a minor shift of the phase center with respect to the position of the Hi-GAL $160\ \mu\text{m}$ clumps.

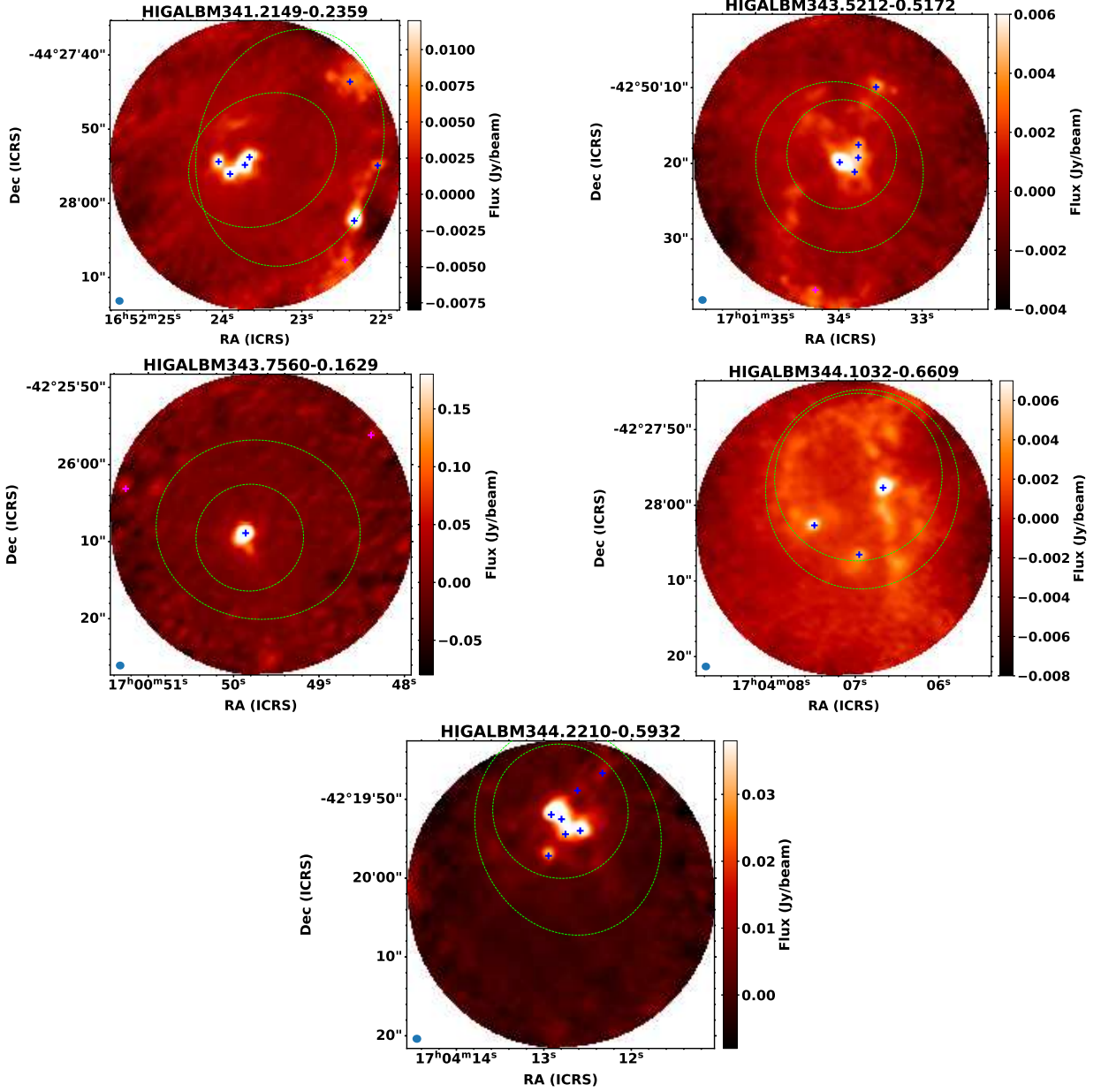


Figure 2. Figure 1 continuum.

2017; Svoboda et al. 2019; Sanhueza et al. 2019; Zhang et al. 2020). However, instead of using a single temperature for the whole sample we have assumed three different dust temperatures that account for the different evolution of our sources. We split the clumps in three groups based on their L/M , following the three evolutionary phases described in Molinari et al. (2016b): $L/M < 1 L_{\odot}/M_{\odot}$, when they are still in a pristine, pre-stellar phase, with temperatures of the innermost regions of the clumps $T < 30$ K; $1 \leq L/M \leq 10 L_{\odot}/M_{\odot}$, when they are forming the first protostars and the temperatures rises to $T \simeq 30$ K; $L/M > 10 L_{\odot}/M_{\odot}$, when a relatively evolved protostar is heating up the dust envelope and the inner cores could have already formed an ultra-compact HII region, with temperatures significantly above 30 K. In particular, some of our fragments may be even warmer than the 40 K used as the highest temperature in the clump

analysis (Elia et al. 2021). At the same time, the mm dust emission traces principally the (relatively) cold dust envelope, therefore we do not expect a significantly higher temperature of the 1.3 mm dust emission observed with ALMA. The temperatures at these scales are expected to vary in the range $15 \leq T \leq 30$ K from pre-stellar to intermediate-mass protostellar fragments (Motte et al. 2022). The mass-averaged dust temperatures in the cores identified at $\simeq 2500$ AU scales in W43-MM2&MM3 are in the range $20 \leq T \leq 65$ K (Pouteau et al. 2022). The fragments identified in the hub-filament systems of Anderson et al. (2021), which resolves spatial scales down to $\simeq 0.03$ – 0.07 pc and are therefore more similar to our objects, span a temperature range $15 \leq T \leq 46$ K. Without data available for lines sensitive to the temperature of the dust envelopes of our fragments, and based on the previous considerations, we fixed the fragment temperatures

T_f (K)	T_{lim} (K)	$M_{f/lim}$
20	10 - 40	2.74 - 0.43
30	10 - 50	4.54 - 0.56
40	20 - 60	2.32 - 0.64

Table 4. *Col. 1:* reference temperature of the dust used to estimate the fragment mass for the scientific analysis; *Col. 2:* range of temperatures used to estimate the mass uncertainties; *Col. 3:* range of $M_{f/lim}$ for the various fragments estimated from Equation 2.

T_f for the three groups to 20 K, 30 K and 40 K respectively. The physical parameters derived for each fragment with our assumptions are listed in Appendix B.

3.2.2 Temperature uncertainties and their implications

The uncertainties on the temperature of the dust envelopes of the fragments are the largest source of uncertainties that can affect our results. In order to quantify these values we assumed an error in the temperature estimation up to 20 K, except for the lowest temperature considered for the group with $L/M < 10 L_\odot/M_\odot$, for which we considered a lower limit of 10 K. The range of temperatures T_{lim} explored for each group are in Table 4.

These assumptions allow us to explore a range of temperatures similar, and even larger than the values observed in other cores/fragments surveys (Pouteau et al. 2022; Anderson et al. 2021). At the same time, we do not expect a particularly warm fragment in extremely young star-forming regions (maximum $T_{lim} = 40$ K for fragments in clumps with $L/M < 1 L_\odot/M_\odot$), neither a particularly cold fragment in very luminous and warmed-up clumps ((minimum $T_{lim} = 20$ K for fragments in clumps with $L/M > 10 L_\odot/M_\odot$).

These temperature limits can be converted into mass limits M_{lim} from Equation 1. In particular, it follows that the mass ratio $M_{f/lim}$ evaluated assuming two different temperatures, T_f and T_{lim} , is equivalent to the ratio of the blackbody part of Equation 1:

$$M_{f/lim} = \frac{M_f}{M_{lim}} = \frac{B_{1.3}(T_{lim})}{B_{1.3}(T_f)} \quad (2)$$

The values of $M_{f/lim}$ for the various T_{lim} are in Table 4. We obtain mass differences of \simeq a factor of 2 and up to $M_{f/lim} \simeq 4.5$ (when considering $T_{lim} = 10K$ instead of $T_f = 30K$). Overall, these temperature variations may significantly affect the mass estimates for each single fragment. These variations are not affecting the statistical studies that we will do in the following sections. As we show in details in Appendix D, we have run a series of Monte Carlo simulations in which we have assigned to each fragment a random temperature within the ranges described before. For each new temperature we have re-evaluated the temperature-dependent parameters described in Section 5.2 and compared the results with those obtained using $T = T_f$. These tests shown that our results, based on the correlation between different quantities, are robust against these temperature variations. Nonetheless, in the analysis in Section 5, where we

will compare the fragment properties with those of the parent clumps, we will split the results in two groups. The ones derived from the spatial distribution of the fragments, which are independent from the dust temperature, and the results that are sensitive to the temperature estimation such as the ones derived from the mass and surface density of the fragments.

3.2.3 Mass completeness limits

A crucial part of the analysis of the properties of these fragments is to understand how good is our recovery of the faintest objects in each clump. The mass completeness limit M_{com} for each clump depends on both the *r.m.s.* of the map and the source distance, which in our sample vary in the ranges $\simeq 0.8$ mJy/beam and $\simeq 15.2$ mJy/beam (Table 2) and $2.0 \leq d \leq 5.5$ kpc (Table 1) respectively.

Note that due to the background-subtracted flux estimation the intensity of the faintest peak that we are able to recover can be significantly lower than the 3σ value of the *r.m.s.* of each map used to identify the peaks in each image. Several tests done with *Hyper* or similar extraction algorithms such as *Cutex* (Molinari et al. 2011) showed that we can assume a conservative estimate of 1σ value of the local *r.m.s.* as the lower limit to the peak emission of a fragment that we can recover in each map (e.g. Molinari et al. 2016a). These flux values can be converted into mass limits assuming that they correspond to the emission of a point-like source. Using Equation 1 and assuming for each clump the dust temperature defined in the previous section, we found M_{com} in the range $0.1 \leq M_{com} \leq 4.7 M_\odot$. These limits are reported in Table 5, together with the minimum recovered mass of the fragments for each clump (M_{min}), estimated as discussed in the previous section, the ratio between these two values (M_{ratio}), and the total number of robust fragments identified in each source $\#_f$. The mass of the least massive fragment is at least 2.2 times higher than the mass limits (and up to $\simeq 72$ times greater for the single massive fragment identified in HIGALBM343.7560-0.1629), suggesting that if more fragments are present in each map, they should be on average several times less massive than the observed ones.

4 FRAGMENTS PROPERTIES

In Figure 3 we show the distribution of the mass of the fragments in our clumps. The grey-dotted vertical lines represent the mass completeness of each clump. The fragment mass distribution covers more than two orders of magnitude, with fragments masses between $0.4 M_\odot$ and $309 M_\odot$ (see Appendix B).

In terms of evolution young, massive clumps are already fragmenting themselves, with the three $70 \mu\text{m}$ -quiet clumps, HIGALBM24.0116+0.4897, HIGALBM28.1957-0.0724 and HIGALBM31.9462+0.0759 breaking into 2, 4 and 4 fragments, respectively, with masses that ranges between $\simeq 2.6$ and $\simeq 32 M_\odot$. These numbers are roughly in agreement with the results of ALMA surveys specifically designed to investigate the properties of $70 \mu\text{m}$ -quiet clumps (Svoboda et al. 2019; Sanhueza et al. 2019), which also have a spatial resolution comparable with the SQUALO survey ($\simeq 0.015$ pc in Svoboda et al. (2019) and $\simeq 0.02$ pc on average in

DESIGNATION	M_{com} (M_{\odot})	M_{min} (M_{\odot})	M_{ratio} ()	$\#_f$
HIGALBM327.3918+0.1996	1.20	7.13	6.0	9
HIGALBM327.4022+0.4449	3.12	45.84	14.7	5
HIGALBM331.1314-0.2438	4.74	104.49	22.0	2
HIGALBM332.6045-0.1674	0.25	2.71	10.6	2
HIGALBM338.9260+0.6340	1.33	9.48	7.1	4
HIGALBM341.2149-0.2359	0.37	0.81	2.2	7
HIGALBM343.5212-0.5172	0.16	0.71	4.3	5
HIGALBM343.7560-0.1629	1.02	73.35	71.9	1
HIGALBM344.1032-0.6609	0.11	0.42	3.8	3
HIGALBM344.2210-0.5932	0.26	1.27	5.0	7
HIGALBM24.0116+0.4897	1.51	8.95	5.9	2
HIGALBM28.1957-0.0724	0.87	2.57	2.9	4
HIGALBM31.9462+0.0759	0.98	2.61	2.7	4

Table 5. Mass completeness values for each source. *Col 1:* Clump designation; *Col 2:* Mass completeness limit M_{com} derived for each clump and based on the $r.m.s.$ of each map as described in Section 3.2.3; *Col 3:* Minimum mass M_{min} identified in each clump in our ALMA Band6 maps; *Col 4:* M_{com}/M_{min} ratio; *Col 5:* number of identified fragments in each clump.

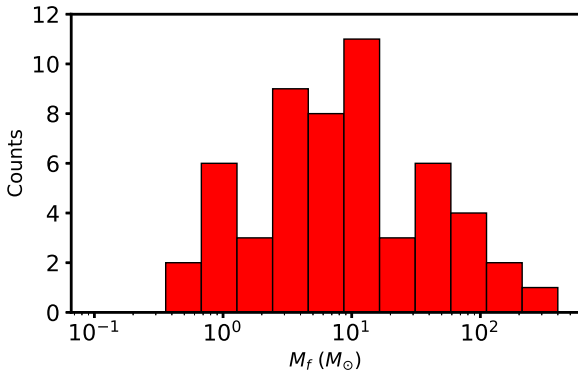


Figure 3. Mass distribution of the 55 fragments identified in our 13 SQUALO sources.

Sanhueza et al. (2019), compared to $\simeq 0.028$ pc on average in this work) and found the vast majority of their clumps already fragmented. Our results confirm that a certain degree of fragmentation is already present at the very early stages of formation, although some isolated examples of massive, dense and young objects have been observed in the literature, such as Core #6 in W43-MM1, with $60 M_{\odot}$ in $\simeq 1300$ AU (Nony et al. 2018).

In the more evolved regions we found the most massive objects, with 4 fragments with masses above $100 M_{\odot}$. These values are higher than those measured in recent ALMA surveys of evolved star-forming regions such as CORE (Beuther et al. 2018) and ALMA-IMF (Motte et al. 2018; Pouteau et al. 2022), which reach masses up to $\simeq 40 M_{\odot}$ (in the CORE survey, Beuther et al. 2018) and $\simeq 70 M_{\odot}$ (in W43 MM2&MM3 in ALMA-IMF, Pouteau et al. 2022). However, a direct comparison with these projects is not straightforward: there are differences in the source extraction algorithms, the specifics of the ALMA observations and the estimation of the dust mass (due to different assumptions of the dust temperatures

and of the parameters used in Equation 1). In particular, the spatial resolution of those surveys is higher than that of SQUALO ($\simeq 1000$ AU in CORE, Beuther et al. (2018), and $\simeq 2000$ AU in ALMA-IMF, Motte et al. (2022)), compared to $\simeq 4700$ AU on average of this work, see Table 2). Both these works have identified objects smaller than the ones found in our survey.

The impact of the spatial resolution on the identification of the smallest fragments is also evident from the results of the ALMA survey of massive progenitors in ATLASGAL (Csengeri et al. 2017). These authors have looked at the fragmentation properties in a sample of 35 objects observed with a resolution ≥ 0.06 pc, \simeq a factor of 2 lower than the resolution of SQUALO. At these scales Csengeri et al. (2017) found well resolved fragments with masses up to $400 M_{\odot}$, suggesting that there are several intermediate steps in the hierarchical process. In several clumps these authors also found evidence of a single, monolithic fragment, which is likely to separate in smaller entities if observed at higher resolution, as observed in this work and in other surveys (e.g. Beuther et al. 2018; Svoboda et al. 2019; Sanhueza et al. 2019). In fact, even some of our objects may further fragment into smaller objects, and this could be particularly true for those fragments that have been observed in the more evolved regions. This possibility will be further discussed in Section 5.

4.1 A peculiar source: HIGALBM343.7560-0.1629

Among the evolved clumps we also find our single example of an object that does not fragment, HIGALBM343.7560-0.1629 ($L_{cl}/M_{cl} = 14.7 L_{\odot}/M_{\odot}$). It contains one of the most massive object we identified, with $M \simeq 73 M_{\odot}$. This source is one of the massive protoclusters observed with ALMA at 1.3mm in the work of Csengeri et al. (2017), but with a spatial resolution of $\simeq 6840$ AU (re-scaled at the distance adopted in this work for HIGALBM343.7560-0.1629, 2.0 kpc, see Table 5) compared to the $\simeq 2130$ AU of our data in the work. It is a good example of the hierarchical process that connects clumps to actual cores, with "intermediate" objects such as the ones observed in the Csengeri et al. (2017) sample and, at three times higher resolution, at the SQUALO resolution. In the work of Csengeri et al. (2017) they identified two sources in the field, MM1 (corresponding to our fragment) and MM2, with masses of $115.5 M_{\odot}$ and $20.2 M_{\odot}$ respectively. Our new data however suggest that our single fragment in this clump is likely truly single at the scales of our observations, and source MM2 is actually part of the diffuse emission associated with the main MM1 source (see their Figure A1 in comparison with our Figure 1). If a second fragment would be present, it should be less massive than the mass completeness limit discussed in Section 3.2.3, which for this source is $\simeq 1.0 M_{\odot}$ (Table 5). Therefore, if there are other fragments at the SQUALO scales those have to be at least 20 times less massive than the value estimated for MM2, and 70 times less massive than our identified fragment. However HIGALBM327.3918+0.1996, the most distant protostellar clump in our sample, is located $\simeq 5.2$ kpc away from us and it shows several fragments (with masses in the range $9 \leq M \leq 45 M_{\odot}$). With $L_{cl}/M_{cl} \simeq 12.6 L_{\odot}/M_{\odot}$, it is in terms of evolution comparable to HIGALBM343.7560-0.1629. At the same time all our $70 \mu\text{m}$ -quiet objects are located further away than HIGALBM343.7560-0.1629 and they

all already show some degree of fragmentation. The behaviour of this source is therefore peculiar with respect to the rest of the sample. It is possible that some particular mechanism is in place in HIGALBM343.7560-0.1629 that allows the condensation of the different fragments observed in 70 μm -quiet objects into a single object, for example a significant role of magnetic fields, as suggested by e.g. [Fontani et al. \(in 2016\)](#) or [Palau et al. \(2021\)](#). A more detailed investigation of this peculiar source and its properties is beyond the scope of this work.

4.2 Jeans analysis

We start to investigate the driver of the fragmentation at the scales probed by our observations by looking at the Jeans values of our objects. If the fragmentation is thermally driven, we would expect the separation between fragments and the mass of the fragments to be compatible with the Jeans length $\lambda_{J,cl}$ and Jeans mass $M_{J,cl}$ of the clumps respectively, defined as:

$$\lambda_{J,cl} = \sigma_{th} \left(\frac{\pi}{G\rho_{cl}} \right)^{1/2}, \quad (3)$$

and

$$M_{J,cl} = \frac{4\pi\rho_{cl}}{3} \left(\frac{\lambda_{J,cl}}{2} \right)^3, \quad (4)$$

where ρ_{cl} is the average density of the host clumps (assumed as perfect spheres and derived from mass M_{cl} and radius R_{cl} of the clumps, Table 3), and σ_{th} is their thermal velocity dispersion. The value of σ_{th} is evaluated as $\sigma_{th} = [k_B * T_{cl}/(\mu m_H)]^{1/2}$ with T_{cl} the clump temperature and $\mu = 2.33$, assuming that the thermal velocity dispersion is dominated by a gas mixture of H_2 and He.

To define a value for the separation between the fragments in each clump we measured $d_{min,2D}$ (where the 2D underlines that this value is not corrected for any projection effect), the minimum distance between each fragment and its closest neighbourhoods, using a minimum spanning tree algorithm (MST, [Barrow et al. 1985](#)). We then introduced the a-dimensional quantity $\lambda_{J_r,2D}$, defined as the ratio of $d_{min,2D}$ to the thermal Jeans length of the clump:

$$\lambda_{J_r,2D} = d_{min,2D}/\lambda_{J,cl} \quad (5)$$

In order to account for the distribution of the positions of the fragments along the line of sight (LOS) we perform a set of Monte Carlo simulations, similar to the procedure described in [Svoboda et al. \(2019\)](#). In practice, for a given pair of fragments we extracted a random distance along the LOS from a Gaussian distribution centered on zero and with a variance dispersion equal to one third of the clump radius at 160 μm (therefore, there is a 3σ possibility that the maximum distance of the two fragments is equal to the 160 μm clump size). For each pair of fragments we made 10000 realizations of their relative distances along the LOS and we have taken the mean value of the derived 3D-distances as the representative one. We considered the minimum fragment separation for each clump ($d_{min,3D}$) and we refer to the ratio of this value to the thermal Jeans length as $\lambda_{J_r,3D}$. Taking

into account the projection effects, $\lambda_{J_r,3D}$ varies in the range $1.06 \leq \lambda_{J_r,3D} \leq 7.04$, not consistent on average with pure thermal fragmentation, suggesting that some support against the gravitational collapse at these scales is also likely in these objects.

If we introduce the non-thermal support against the fragmentation in the calculations, and substitute σ_{th} with the clumps non-thermal velocity dispersion σ_{nth} to estimate the Jeans length, we obtain values in the range $0.28 \leq \lambda_{J_r,nth,3D} \leq 1.47$. In particular, except for the source HIGALBM332.6045-0.1674, for which this value is $\lambda_{J_r,nth,3D} = 1.47$, for all the other sources $\lambda_{J_r,nth,3D} < 1$, smaller than "pure" non-thermal fragmentation values, which would give $\lambda_{J_r,nth,3D} = 1$. The Jeans parameters related to the analysis of the Jeans length for each clump are given in Table 6.

Similarly to what we have done for the Jeans length analysis, the comparison of the Jeans mass $M_{J,cl}$ with the value of the most massive fragment $M_{f,max}$ in each clump, shows that for all these clumps the value $M_{J_r} = M_{max}/M_{J,cl} > 1$, and in some cases $M_{J_r} \gg 1$. If we substitute σ_{th} with the clumps non-thermal velocity dispersion σ_{nth} to estimate the Jeans mass, we obtain values $0.01 \leq M_{J_r,nth} \leq 0.93$, with the exception of HIGALBM343.7560-0.1629 and HIGALBM331.1314-0.2438 that have $M_{J_r,nth} \simeq 1.7$, supporting the hypothesis that some mechanism is in place in these sources to support the fragmentation of the clump. All the parameters related to the analysis of the Jeans mass properties of our objects are given in Table 7.

These results suggest that the fragmentation properties observed at the resolution probed by our observations could partially be supported by the turbulent cascade, but part of the observed non-thermal motions could also originate from a different mechanism (such as the gravitational collapse). We will further discuss these findings in the next section.

5 FRAGMENTS VS. CLUMP PROPERTIES

In this section we investigate the possible correlations between the properties of the clumps and of their fragments as a function of the clump evolution. Also, whenever possible, we combine our datasets with ancillary data taken from the literature to put our results in a broader context.

Our sample of clumps is not large enough to allow the use of statistical tools such as the principal component analysis. Instead, we calculated the Pearson's correlation coefficient ρ for each pair of quantities, which estimates the level of linear correlation between our data (from $\rho = -1$ and $\rho = 1$, which express total anti-correlation and total correlation, respectively), using the Python package `Pymccorrelation` ([Privon et al. 2020](#)). We considered the following parameters for the clumps: mass M_{cl} , L/M ratio L_{cl}/M_{cl} , surface density Σ_{cl} , mass accretion rate \dot{M}_{cl} and virial parameter $\alpha_{vir,cl}$; the following ones for the fragments: the number of fragments in each clump $\#_f$, the minimum 2D (3D) distances between fragments, $d_{min,2D}$ ($d_{min,3D}$), the total mass of fragments in each clump M_f , the mass and surface density of the most massive and of the densest fragment in each clump, $M_{f,max}$ and $\Sigma_{f,max}$, respectively. We also considered the following parameters that combine the clump and fragment properties: the instantaneous clump formation efficiency (CFE), defined

DESIGNATION	$d_{min,2D}$ (pc)	$d_{min,3D}$ (pc)	σ_{th} (km s ⁻¹)	$\lambda_{J,cl}$ (pc)	$\lambda_{J_r,2D}$	$\lambda_{J_r,3D}$	σ_{nth} (km s ⁻¹)	$\lambda_{J,nth}$ (pc)	$\lambda_{J_r,nth,2D}$	$\lambda_{J_r,nth,3D}$
HIGALBM327.3918+0.19	0.030	0.077	0.28	0.025	1.23	3.13	1.44	0.124	0.24	0.62
HIGALBM327.4022+0.44	0.030	0.075	0.32	0.025	1.22	3.05	1.66	0.127	0.24	0.59
HIGALBM331.1314-0.24	0.037	0.081	0.33	0.018	2.02	4.43	2.04	0.113	0.33	0.72
HIGALBM332.6045-0.16	0.136	0.142	0.26	0.020	6.73	7.04	1.26	0.097	1.41	1.47
HIGALBM338.9260+0.63	0.073	0.096	0.26	0.023	3.17	4.15	1.66	0.147	0.50	0.65
HIGALBM341.2149-0.23	0.021	0.065	0.27	0.045	0.46	1.43	1.09	0.181	0.12	0.36
HIGALBM343.5212-0.51	0.025	0.051	0.28	0.025	0.99	1.98	1.25	0.116	0.22	0.44
HIGALBM343.7560-0.16	0.000	0.000	0.29	0.018	0.00	0.00	1.22	0.076	0.00	0.00
HIGALBM344.1032-0.66	0.069	0.084	0.28	0.028	2.51	3.04	1.64	0.164	0.42	0.51
HIGALBM344.2210-0.59	0.014	0.035	0.35	0.033	0.41	1.06	1.33	0.128	0.11	0.28
HIGALBM24.0116+0.489	0.083	0.115	0.20	0.029	2.84	3.94	0.91	0.137	0.61	0.84
HIGALBM28.1957-0.072	0.127	0.182	0.21	0.056	2.27	3.25	1.07	0.281	0.45	0.65
HIGALBM31.9462+0.075	0.071	0.105	0.19	0.024	2.97	4.39	1.19	0.149	0.48	0.70

Table 6. Parameters derived from the length Jeans analysis described in Section 4. *Col.1*: Clump designation; *Cols.2-3*: minimum distance between fragments derived with the MST algorithm, uncorrected and corrected for the 3D projection effects along the LOS, respectively; *Col.4*: sound speed derived for each clump; *Col.5*: clump thermal Jeans length; *Cols.6-7*: ratio between the measured Jeans length in each clump and the thermal Jeans length, uncorrected and corrected for the 3D projection effects along the LOS, respectively; *Col. 8*: clump non-thermal sound speed; *Cols. 9-11*: same as Cols. 5-7 but assuming non-thermal velocity dispersion (i.e. substituting σ_{th} with σ_{nth}).

DESIGNATION	$M_{f,Max}$ (M _⊙)	$M_{J,cl}$ (M _⊙)	M_{J_r}	$M_{J,nth}$ (M _⊙)	$M_{J_r,nth}$
HIGALBM327.3918+0.19	44.9	0.76	58.83	98.60	0.455
HIGALBM327.4022+0.44	124.7	0.99	125.61	133.72	0.932
HIGALBM331.1314-0.24	309.3	0.78	396.28	179.44	1.724
HIGALBM332.6045-0.16	18.0	0.54	33.60	58.68	0.307
HIGALBM338.9260+0.63	68.9	0.60	113.76	154.89	0.445
HIGALBM341.2149-0.23	10.3	1.30	7.92	82.08	0.126
HIGALBM343.5212-0.51	2.1	0.73	2.90	69.20	0.031
HIGALBM343.7560-0.16	73.3	0.59	125.11	43.48	1.687
HIGALBM344.1032-0.66	2.4	0.80	3.04	168.27	0.014
HIGALBM344.2210-0.59	9.2	1.54	5.96	86.29	0.106
HIGALBM24.0116+0.489	31.9	0.42	75.00	43.38	0.734
HIGALBM28.1957-0.072	7.7	0.97	7.94	123.25	0.063
HIGALBM31.9462+0.075	25.9	0.33	77.53	80.76	0.321

Table 7. Parameters derived from the mass Jeans analysis described in Section 4. *Col.1*: Clump designation; *Col.2*: mass of the most massive fragment in each clump; *Col.3*: clump Jeans mass; *Col.4*: ratio between the Jeans mass and the mass of the most massive fragment in each clump. *Cols. 5-6*: same as Cols. 3-4 but assuming non-thermal velocity dispersion (i.e. substituting σ_{th} with σ_{nth}).

as the ratio between the total mass of the fragments in each clump and the mass of the clump (e.g. Anderson et al. 2021), and the ratio between the clump 2D Jeans length (3D corrected) and the minimum distance between fragments in each clump, $\lambda_{J_r,2D}$ ($\lambda_{J_r,3D}$).

In Figure in Appendix C we show the correlation matrix (or heatmap) of all these quantities, colour-coded with the value of the Pearson's correlation parameter (reported in each cell). In Appendix E we report the values of ρ for all the pairs we considered with the probability that the null hypothesis is true (the p-value) and the 95% confidence interval (CI 95%) for each pair of parameters.

Before going into the analysis of the results presented in the heatmap in Appendix C, we want to caution that "correlation is not causation", in particular for our relatively small dataset. A high (or low) value of the Pearson coefficient in a given pair of parameters may not be due to some physical process and should be taken "cum grano

salis". In particular, the estimation of the uncertainties plays a role to determine the reliability of each Pearson's coefficient (and the corresponding estimation of the p-value). For all the parameters analysed in this work we considered an uncertainties equal to 20% of the measured value. In most cases this is a conservative estimation, for example the clump properties such as the mass have uncertainties quoted in the Elia et al. (2021) catalogue below 10% for 9 out of 13 of our sources. For three sources, HIGALBM341.2149-0.2359, HIGALBM24.0116+0.4897 and HIGALBM28.1957-0.0724 the quoted uncertainties are $\simeq 86\%$, $\simeq 40\%$ and $\simeq 40\%$ respectively. The quoted mass uncertainty for source HIGALBM31.9462+0.0759 in the Hi-GAL catalogue is unrealistically higher because no distance were assigned to the source. Note however that the source mass estimated for this source in Traficante et al. (2017) differs by only 3% from the mass estimation in Elia et al. (2021).

Similarly, the uncertainties on the source distances, which

will affect both clumps and fragments properties, are $\leq 15\%$ for 10 sources and equal to 20% for the other three (HIGALBM343.7560-0.1629, HIGALBM344.1032-0.6609 and HIGALBM344.2210-0.5932 [Mège et al. 2021](#)).

Even accounting for these uncertainties and limitations, there are some general considerations that can be drawn from the correlation matrix shown in the heatmap in Appendix C, in particular when drawn by comparing the correlation coefficients of multiple pairs of parameters, or when including results from other surveys from the literature. These conclusions will eventually be corroborated by further investigation on larger samples of massive clumps undergoing global collapse (as the one that could be provided by the ALMAGAL survey).

5.1 Fragments number and relative distance vs. clump properties

In this section we will describe the results derived from the properties of the fragments that are independent from their dust temperature.

The first pair of parameters that we consider is the degree of fragmentation as a function of the evolutionary phase of these clumps (defined by L_{cl}/M_{cl}), shown in Figure 4. Overall, these two quantities are mildly correlated ($\rho = 0.37$ with a p -value of 0.22). This diagram suggests that the degree of fragmentation at these scales is not simply regulated by the evolutionary phase of each object: we found sources with $L_{cl}/M_{cl} > 10$ that embed a single fragment (HIGALBM343.7560-0.1629, Section 4.1), sources that embed 2 or more fragments and up to 9 fragments in HIGALBM327.3918+0.1996, the most fragmented clump of our sample. However, one interesting result to note is that, as already discussed in Section 4, at very early stages of formation the systems are already fragmented.

Figure 5 shows the correlation between the number of fragments and the Jeans ratio $\lambda_{J,r,3D}$, colour-coded for the clump evolution. These parameters present the highest degree of (anti)correlation with the number of fragments, $\#_f$, with $\rho = -0.67$, and this (anti-)correlation is more solid than the previous one, with p -value=0.02 (assuming an uncertainty of 20% on the estimation of the Jeans ratio, as discussed in the previous Section).

This plot suggests that the number of fragments is lower at high values of $\lambda_{J,r,3D}$ and it increases as the system approaches the thermal Jeans scale, $\lambda_{J,r,3D} = 1$.

This last result could be a consequence of the number of fragments observed in each clump: it is expected that the higher the number of fragments in each object, the shorter the minimum distance between them (and therefore the smaller $\lambda_{J,r,3D}$ for clumps of comparable thermal Jeans length, see Table 6). However, this result is more instructive if we put it in an evolutionary context: as showed in Figure 5, the clumps with the lower values of $\lambda_{J,r,3D}$ are among the most evolved of our sample (with the exception of HIGALBM331.1314-0.2438, which embeds the most massive fragment we have identified). This trend is further confirmed by the plot in Figure 6, where we report $d_{min,2D}$ as a function of the L/M of the parent clumps. It is remarkable the lack of points in the bottom-left corner of the plot, i.e. the lack of points with low L_{cl}/M_{cl} and low $d_{min,2D}$. The value of $d_{min,2D}$ for the points with $L_{cl}/M_{cl} < 10$ is always above the resolution

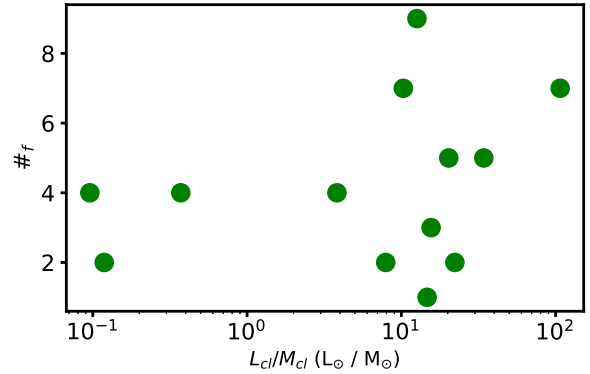


Figure 4. Clumps L/M , indicator of their evolutionary phases, as a function of the number of fragments identified in each clump.

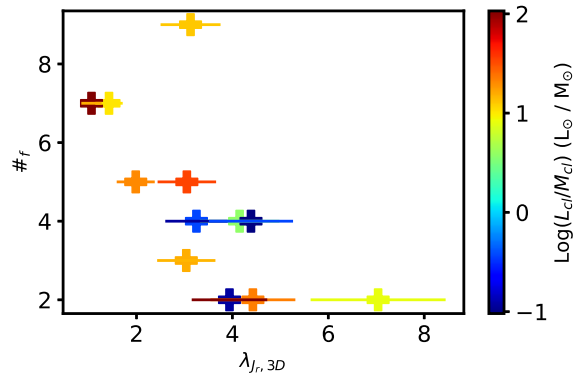


Figure 5. Ratio of the minimum fragment separation and the thermal Jeans length, corrected for the 3D projection effects, $\lambda_{J,r,3D}$, as a function of the number of fragments in each clump. The distribution is colour-coded for the clumps L/M .

limit of our survey ($\simeq 0.01 - 0.04$ pc, see Table 2). These results suggest that 1) each of the fragments in the youngest clumps may have already produced multiple cores very close to each other, below our resolution limits, or 2) these fragments will get closer with time (and eventually merge or keep fragmenting). Here we have considered the relation between L_{cl}/M_{cl} and $d_{min,2D}$ since we report for comparison also the objects studied in the CORE survey ([Beuther et al. 2018](#)). The CORE survey targeted evolved regions in the northern sky with NOEMA to resolve down to $\simeq 1000$ AU resolution objects up to 6 kpc away from us ([Beuther et al. 2018](#)), $\simeq 4 - 5$ times better than our resolution. Since a few of their fragments have $d_{min,2D,core}$ smaller than our resolution, it is possible that some of our fragments will further separate down to $\simeq 1000$ AU resolution. In particular, this could be true for the more evolved objects: all CORE clumps in fact have $L/M > 10$, but note that in their survey all but one of the 8 fragments with $d_{min,2D,core} < 2500$ AU have $L/M > 70 L_{\odot}/M_{\odot}$, which corroborates the hypothesis that the cores in the most evolved objects are on average closer to each other.

All these results can be interpreted to favour a model where sources evolve in a highly dynamical *clump-fed*, gravo-turbulent scenario, in which the high values of $\lambda_{J,r,3D}$ (and low values of $d_{min,2D}$) observed in young clumps may just

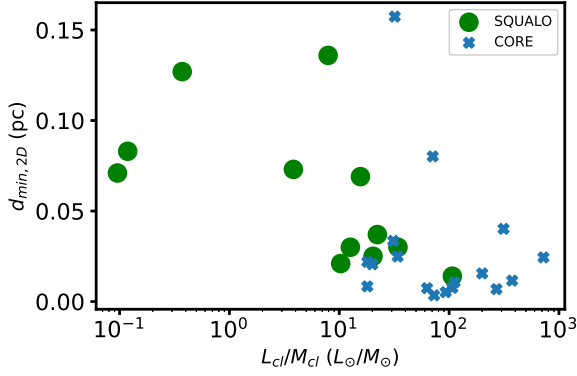


Figure 6. Clump L/M , indicator of their evolutionary phases, as a function of the minimum 2D distance between fragments identified in each clump. The green circles is the SQUALO sample, and the blue crosses is the CORE sample taken from Beuther et al. (2018).

be a step in the hierarchical evolution. The process starts with the formation of a few non-thermally supported fragments in which there is likely an interplay between gravity and turbulence. With time, the gravitational contraction takes over and the fragments get closer, merge and/or further fragment into more thermally supported objects. In sources such as HIGALBM343.7560-0.1629 and others with few (≤ 3) fragments other factors such as magnetic fields may play a more relevant role than in other clumps (Palau et al. 2021), leading to a magnetically-regulated collapse that supports, or suppresses the fragmentation (Fontani et al. 2016). These hypotheses could be tested against simulations of massive star-forming clumps such as the ones produced by Lee & Hennebelle (2016).

5.2 Fragments physical properties vs. clump properties

In this section we will discuss the results derived from the properties of the fragments that are dependent on their dust temperature, such as their mass and surface density.

In a *clump-fed* scenario the accretion rate from clump to core is $\dot{m}_{cl} \neq 0$ (Peretto et al. 2020). The opposite, or at least no direct correlation between core accretion and clump accretion is expected in a *core-fed* scenario. A consequence of the *clump-fed* model is therefore a correlation between the core/fragment mass and the clump mass, which are expected to be dynamically correlated (Anderson et al. 2021). Our sample has been chosen to show evidence of clump-scale accretion rate from single-dish surveys, therefore we expected to observe such correlation. As shown in the heatmap in Appendix C, we indeed measure a tight correlation between the mass and density of the clumps and the mass and density of the fragments: clumps with the highest surface density also form the most massive fragments and with the highest surface density.

To put these results more in context, we have compared our sample with three others taken from the literature: the $70 \mu\text{m}$ quiet objects observed in Sanhueza et al. (2019) and Svoboda et al. (2019) ALMA surveys, plus the 6 hub-filament systems in infrared-dark clouds examined in Anderson et al. (2021). The physical properties of the Sanhueza et al. (2019)

and Anderson et al. (2021) surveys have been extracted from their works. For the Svoboda et al. (2019) sample the physical properties of the fragments have been derived from their fluxes, which have been converted into mass using Equation 1 and the same parameters considered for our $70 \mu\text{m}$ -quiet objects. We initially tried to re-evaluate the clump properties of these samples from the Elia et al. (2021) catalogue, for a consistent comparison between all samples. However, not all the clumps were identified in the Elia et al. (2021) catalogue and eventually with a non well-defined distances. Therefore, we decided to consider the clump parameters discussed in the literature, with the note of caution that the comparisons between different catalogues may suffer from biases introduced by the various extraction algorithms and approaches used to derive the physical parameters in the various works (see e.g. the results in Kauffmann & Pillai 2010).

The relation between mass of the clumps and mass of inner fragments for all the surveys is showed in Figure 7. The error bars in the SQUALO sample derive from the temperature uncertainties as described in Section 3.2.2. The filament-hub system in Anderson et al. (2021) is colour-coded according to the temperature of the cores as estimated in Anderson et al. (2021), that we assume as evolutionary indicator of their sample.

Also combining different data sets there is a general indication that these quantities are correlated. As consequence of this plot, we observe a good degree of correlation between the CFE and mass of the fragments ($\rho = 0.65$, p-value=0.016, Appendix C): the clumps with highest instantaneous formation efficiency embed the most massive fragments in our survey (see Figure 7), in agreement with the results (at slightly larger scales) of Csengeri et al. (2017).

Similarly, in Figure 8 we show the relation between the clump surface density and the surface density of the densest fragment for all surveys. In particular, our new data and the survey of Anderson et al. (2021), the only two samples in this plot with objects spanning different evolutionary phases, show an intrinsic good correlation of these two quantities (Pearson coefficient $\rho = 0.60$ for our survey, Appendix C). In both these surveys the youngest objects have among the lowest values of Σ_{cl} and $\Sigma_{f,max}$. It is worth noting that the densest clumps may form the more massive fragments in a shortest amount of time, so, strictly speaking, the $70 \mu\text{m}$ -quiet objects and those with high L_{cl}/M_{cl} and higher Σ_{cl} may be at a similar age. However, statistically speaking young clumps have, on average, lower column density than more evolved clumps, a result interpreted as a result of evolution at clump scales (Svoboda et al. 2016; Elia et al. 2021). Our results and the Anderson et al. (2021) survey suggest a dynamic scenario where both the $70 \mu\text{m}$ -quiet clumps and their fragments increase their density as a function of evolution. In this view, the 3 SQUALO protostellar clumps with $L_{cl}/M_{cl} > 1$ that overlaps in this plot with our $70 \mu\text{m}$ -quiet objects could originate from clumps less dense than the ones observed in the SQUALO, Svoboda et al. (2019) and Sanhueza et al. (2019) surveys.

Interestingly, the accretion rate observed at the clump scales shows only a mild correlation with the properties of the fragments. We observe an indication that higher accretion rates at clump scales feed more mass into the inner fragments ($\rho = 0.44$ and p-value=0.14, see also Figure 9). It is also independent on the number of fragments and on the evolutionary

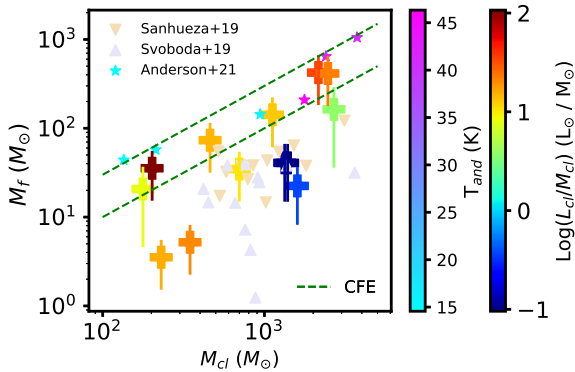


Figure 7. Total mass of the fragments as a function of the mass of the parent clump. The distribution of points from this work is colour-coded for the clumps L_{cl}/M_{cl} and the mass uncertainties derive from the temperature uncertainties as described in Section 3.2.2. We also plot the properties of the samples of $70\ \mu\text{m}$ -quiet objects from Sanhueza et al. (2019, light brown triangles) and Svoboda et al. (2019, light blue triangles), and of massive clumps in hub-filament systems taken from Anderson et al. (2021, colour coded for the temperature of the cores), as discussed in the main text. The green dashed lines are the CFE with efficiencies of 10% (bottom line) and 30% (top line).

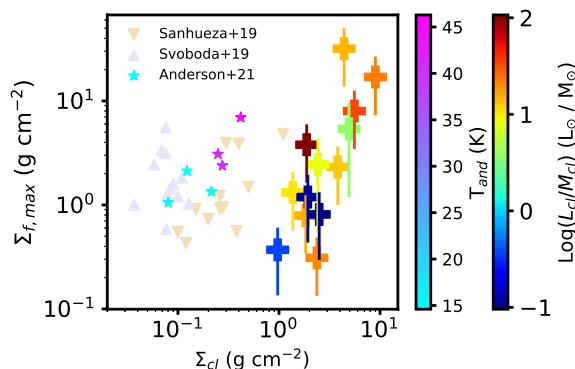


Figure 8. Clump surface density as a function of the surface density of the densest fragment in each clump. The distribution of points from this work is colour-coded for the clumps L_{cl}/M_{cl} . We also plot the properties of the samples of Sanhueza et al. (2019, light brown triangles), Svoboda et al. (2019, light blue triangles), and Anderson et al. (2021, colour coded for the temperature of the cores), as discussed in the main text.

stage of the clump (Appendix C). The large-scale accretion seems to feed either one or more objects independently from the rate of accretion (and the clump evolution). It is also possible that the parsec-scale accretion is feeding the intra-clump sub-filaments that we can see in our images (Figures 1 and 2) and that could be the channels towards which the accretion onto the fragments occurs. In this case, a direct correlation should be found between the accretion at the clump scales and the accretion onto the sub-filaments system. A detailed study of the accretion properties in the intra-clump gas using ALMA Band 3 data in correlation with the accretion properties at the clump scales is the subject of a forthcoming SQUALO paper (Traficante et al. *in prep.*).

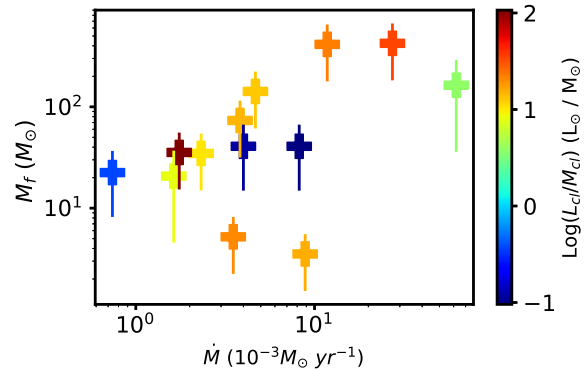


Figure 9. Total mass of the fragments as a function of the clump accretion rate \dot{M} in each clump. The distribution is colour-coded for the clumps L_{cl}/M_{cl} .

The last correlation we will discuss is between the virial parameter of the clumps ($\alpha_{vir,cl}$) and the mass of our fragments. An anti-correlation between α_{vir} and M in massive objects has been discussed several times in the literature, with a typical behaviour $\alpha_{vir} \propto M^{-\delta}$ with $\delta \simeq 0.5$ (Kauffmann et al. 2013; Urquhart et al. 2018; Traficante et al. 2018b). The origin of this anti-correlation is not yet understood. It may be a confirmation that the most massive clumps are more gravitationally bound and the gravitational potential overwhelms the local turbulence (Ballesteros-Paredes et al. 2011), or it may be an observational bias, as these clumps should collapse maintaining a near-virial equilibrium state, either due to a bias in the observations of the gas kinematics (Traficante et al. 2018c) or a combination of several systematic (Singh et al. 2021). The thirteen clumps of our survey also show a good anti-correlation ($\rho = -0.68$, Appendix C), with $\delta \simeq 0.54$, in line with the previous observations given the large intrinsic scatter in the relatively small sample. In Figure 10 instead we show the relation between the virial parameter at the clump scales and the mass of the inner fragments. Therefore, these two parameters are now derived from independent dataset. This diagram shows an anti-correlation, with a Pearson’s coefficient of $\rho = -0.41$ and $\delta \simeq 0.27$. This result support our previous interpretation, i.e. that fragments are fed by their native clumps. If there is a bias in the estimation of the virial parameter of these clumps, this relation simply confirms that the mass of the fragments is tightly connected with the mass of the parental clumps, since they independently produce a similar $\alpha_{vir} \propto M$ relation. Alternatively, this relation implies that the stronger the gravitational potential of the clumps, the bigger the mass of the inner fragments fed by their reservoir. It is worth noting that the mass of the fragments for the three $70\ \mu\text{m}$ -quiet clumps is below the values expected from the average fit in this diagram. This may be a further indication that fragments form at early stages and they will keep accreting with time.

6 CONCLUSIONS

In this work we have presented the first results from the SQUALO (Star formation in QUIescent And Luminous Objects) survey. SQUALO is an ALMA 1 mm and 3 mm survey

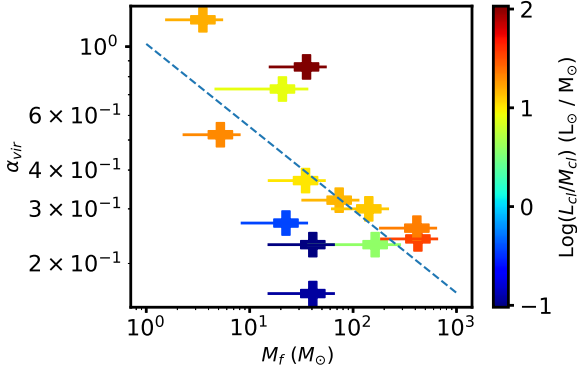


Figure 10. Virial parameter of the clump as a function of the mass of the fragments in each clump. The distribution is colour-coded for the clumps L_{cl}/M_{cl} . The blue line is the best power-law fit of the distribution, which gives an exponent $\delta \simeq -0.27$.

of 13 massive star-forming clumps at various evolutionary phases, from young $70 \mu\text{m}$ -quiet up to evolved HII regions, all selected to exhibit signs of large, parsec scale infall motions. In this first paper we have presented the catalogue of objects in the survey and we have analyzed the properties of the fragments identified in the ALMA 1 mm dust continuum data in correlation with the properties of the parent clumps. The fragments have been extracted in the primary beam corrected maps using the *Hyper* algorithm. A total of 55 robust fragments have been identified in the ALMA images of the 13 SQUALO clumps, 51 of them within the $250 \mu\text{m}$ Hi-GAL footprint and 44 within the $160 \mu\text{m}$ footprint.

The main results of this work are the following:

- 12 out of 13 sources show some degree of fragmentation, with up to 9 fragments in source HIGALBM327.3918+0.1996. Given the resolution of our survey (from $\simeq 0.01$ pc up to $\simeq 0.04$ pc at the distance of the farthest source of our sample, $d = 5.5$ kpc), we expect that some of these fragments will be resolved into smaller objects, as observed in higher resolution images (e.g. Avison et al. 2016). HIGALBM343.7560-0.1629 embeds one of the most massive fragment of our sample, with a mass $M \simeq 73 M_{\odot}$, and does not show any other fragment down to the minimum detectable mass that for this clump is equal to $\simeq 1.0 M_{\odot}$.

- All $70 \mu\text{m}$ -quiet sources are already fragmented into 2 or 4 pieces, which excludes the existence of common isolated, massive pre-stellar cores, in agreement with the findings of Svoboda et al. (2019) and Sanhueza et al. (2019).

- The ratio between the Jeans length of the fragments and the thermal Jeans length, corrected for the 3D-projection effects, $\lambda_{J,r,3D}$, decreases as the number of fragments in each clump increases. Also, the youngest clumps in our sample have on average the highest values of $\lambda_{J,r,3D}$, and only the more evolved ones approaches values of $\lambda_{J,r,3D}$ close to unity (i.e. the expected value in case of pure thermal Jeans fragmentation). Similarly, the minimum 2D distance between fragments appears to decrease with the clumps evolution, a result also supported by the fragmentation properties observed in the clumps of the CORE survey (Beuther et al. 2018). We interpret these numbers as the effect of a gravo-turbulent, hierarchical process: massive clumps initially pro-

duce non-thermally supported fragments which get closer with time and eventually continue to internally fragment until they reach the thermal fragmentation level ($\lambda_{J,r,3D} \simeq 1$). Clumps with a low degree of fragmentation at various scales may represent those cases where the local turbulence play a major role in the process and they are likely supported by magnetic fields, which can limit or completely suppress the fragmentation process (Palau et al. 2021).

- The mass and surface density of the fragments are tightly correlated with the mass and surface density of the parent clumps: the most massive fragments are embedded in the most massive clumps, and the instantaneous clump formation efficiency CFE is higher in clumps with higher fragment mass. The data shows a possible evolutionary path where clump surface density and the density of the fragments increase from $70 \mu\text{m}$ -quiet objects to more evolved regions. These trends are in agreement with Galactic Plane surveys of clumps which demonstrated that their surface density increases with evolution (Svoboda et al. 2016; Elia et al. 2021), and they are also observed at the fragment scales in the ALMA survey of filament-hub systems at various evolutionary phases (Anderson et al. 2021).

- We found an indication that the high accretion rates measured at the clump scales produces more massive fragments (correlation coefficient $\rho = 0.44$). The accretion rate is also independent from the number of fragments identified at the various evolutionary phases. A detailed analysis of the infall properties at clump and fragment scales will be the topic of a dedicated SQUALO work.

- The anti-correlation observed in several surveys between the virial parameter and the mass of the clumps, $\alpha_{vir} \propto M^{-\delta}$, with $\delta \simeq 0.5$, is also observed in our sample. We have also combined the virial parameter of the clumps with the mass of the fragments, building an α_{vir} vs. M relation from independent observations. We found a similar anti-correlation, with a value of $\delta \simeq 0.27$. We interpret this result as a further suggestion that the dynamics of the clumps and of the inner fragments are tightly connected: if there is no bias in the estimation of the virial parameter of our clumps, the more gravitationally bound clumps are the most massive ones and the ones that have build-up the most massive fragments.

We interpret our results as combined evidence in favour of the *clump-fed* scenario, as opposed to the *core-fed* scenario for the formation of massive stars.

Our data suggest a hierarchical, gravo-turbulent process: young, massive clumps initially fragment under the influence of non-thermal motions in interplay with the gravitational fields. With time the fragments condense, gather mass from their surroundings and eventually keep fragmenting until some of them, where the gravitational potential overcome the turbulence, evolve to reach pure thermal Jeans fragmentation. Future surveys such as ALMAGAL, which include a more statistically significant sample of objects, can confirm the scenario that we propose in this work.

ACKNOWLEDGEMENTS

This paper makes use of the following ALMA data: ADS/JAO.ALMA#2018.1.00443.S. ALMA is a partnership of ESO (representing its member states), NSF (USA) and NINS (Japan), together with NRC (Canada), MOST and

ASIAA (Taiwan), and KASI (Republic of Korea), in cooperation with the Republic of Chile. The Joint ALMA Observatory is operated by ESO, AUI/NRAO and NAOJ. A.A. acknowledges support from STFC grants ST/T001488/1 and ST/P000827/1. G.A.F acknowledges support from the Collaborative Research Centre 956, funded by the Deutsche Forschungsgemeinschaft (DFG) project ID 184018867. G.A.F also acknowledges financial support from the State Agency for Research of the Spanish MCIU through the AYA 2017-84390-C2-1-R grant (co-funded by FEDER) and through the "Center of Excellence Severo Ochoa" award for the Instituto de Astrofísica de Andalucía (SEV-2017-0709). R.J.S acknowledges funding from an STFC ERF (grant ST/N00485X/1) and HPC from the DiRAC facility (ST/P002293/1).

DATA AVAILABILITY

The data underlying this article are available in the article and in its online supplementary material.

REFERENCES

- Anderson M., Peretto N., Ragan S. E., et al. 2021, *MNRAS*, **508**, 2964
- Avison A., Quinn L. J., Fuller G., et al. 2016, *MNRAS*, **461**, 136
- Ballesteros-Paredes J., Hartmann L. W., Vázquez-Semadeni E., et al. 2011, *MNRAS*, **411**, 65
- Barrow J. D., Bhavsar S. P., Sonoda D. H., 1985, *MNRAS*, **216**, 17
- Battersby C., Ginsburg A., Bally J., et al. 2014, *ApJ*, **787**, 113
- Beuther H., Mottram J. C., Ahmadi A., et al. 2018, *A&A*, **617**, A100
- Bonnell I. A., Bate M. R., 2006, *MNRAS*, **370**, 488
- Cortes P. C., Hull C. L. H., Girart J. M., et al. 2019, *ApJ*, **884**, 48
- Csengeri T., Bontemps S., Wyrowski F., et al. 2017, *A&A*, **600**, L10
- Di Francesco J., Myers P. C., Wilner D. J., et al. 2001, *ApJ*, **562**, 770
- Elia D., Molinari S., Schisano E., et al. 2017, *MNRAS*, **471**, 100
- Elia D., Merello M., Molinari S., et al. 2021, *MNRAS*, **504**, 2742
- Fontani F., Commerçon B., Giannetti A., et al. 2016, *A&A*, **593**, L14
- Fuller G. A., Williams S. J., Sridharan T. K., 2005, *A&A*, **442**, 949
- Ginsburg A., Bressert E., Bally J., Battersby C., 2012, *ApJL*, **758**, L29
- He Y.-X., Zhou J.-J., Esimbek J., et al. 2015, *MNRAS*, **450**, 1926
- Henshaw J. D., Caselli P., Fontani F. e. a., 2014, *MNRAS*, **440**, 2860
- Jackson J., Rathborne J., Foster J. B., et al. 2013, *PASA*, **30**, e057
- Kauffmann J., Pillai T., 2010, *ApJ*, **723**, L7
- Kauffmann J., Pillai T., Goldsmith P. F., 2013, *ApJ*, **779**, 185
- Könyves V., André P., Men'shchikov A., et al. 2015, *A&A*, **584**, A91
- Könyves V., André P., Arzoumanian D., et al. 2020, *A&A*, **635**, A34
- Lee Y.-N., Hennebelle P., 2016, *A&A*, **591**, A30
- McKee C. F., Tan J. C., 2003, *ApJ*, **585**, 850
- McMullin J. P., Waters B., Schiebel D., et al. 2007, in Shaw R. A., Hill F., Bell D. J., eds, *Astronomical Society of the Pacific Conference Series Vol. 376, ADASS XVI*. p. 127
- Mège P., Russeil D., Zavagno A., et al. 2021, *A&A*, **646**, A74
- Molinari S., Pezzuto S., Cesaroni R., et al. 2008, *A&A*, **481**, 345
- Molinari S., Swinyard B., Bally J., et al. 2010, *PASP*, **122**, 314
- Molinari S., Schisano E., Faustini F., et al. 2011, *A&A*, **530**, A133
- Molinari S., Schisano E., Elia D., et al. 2016a, *A&A*, **591**, A149
- Molinari S., Merello M., Elia D., et al. 2016b, *ApJL*, **826**, L8
- Motte F., Bontemps S., Louvet F., 2018, *ARA&A*, **56**, 41
- Motte F., Bontemps S., Csengeri T., et al. 2022, *A&A*, **662**, A8
- Neupane S., Garay G., Contreras Y., et al. 2020, *ApJ*, **890**, 76
- Nony T., Louvet F., Motte F., et al. 2018, *A&A*, **618**, L5
- Palau A., Ballesteros-Paredes J., Vázquez-Semadeni E., et al. 2015, *MNRAS*, **453**, 3785
- Palau A., Zhang Q., Girart J. M., et al. 2021, *ApJ*, **912**, 159
- Peretto N., Fuller G. A., Duarte-Cabral A., et al. 2013, *A&A*, **555**, A112
- Peretto N., Rigby A., Andre P., et al. 2020, *MNRAS*, **496**, 3482
- Pouteau Y., Motte F., Nony T., et al. 2022, arXiv e-prints, p. [arXiv:2203.03276](https://arxiv.org/abs/2203.03276)
- Preibisch T., Ossenkopf V., Yorke H. W., et al. 1993, *A&A*, **279**, 577
- Privon G. C., Ricci C., Aalto S., et al. 2020, *ApJ*, **893**, 149
- Rosolowsky E. W., Pineda J. E., Kauffmann J., et al. 2008, *ApJ*, **679**, 1338
- Rygl K. L. J., Wyrowski F., Schuller F., et al. 2010, *A&A*, **515**, A42
- Sanhueza P., Contreras Y., Wu B., et al. 2019, *ApJ*, **886**, 102
- Schuller F., Menten K. M., Contreras Y., et al. 2009, *A&A*, **504**, 415
- Shu F. H., 1977, *ApJ*, **214**, 488
- Singh A., Matzner C. D., Friesen R. K., et al. 2021, arXiv e-prints, p. [arXiv:2108.05367](https://arxiv.org/abs/2108.05367)
- Smith R. J., Longmore S., Bonnell I., 2009, *MNRAS*, **400**, 1775
- Svoboda B. E., Shirley Y. L., Battersby C., et al. 2016, *ApJ*, **822**, 59
- Svoboda B. E., Shirley Y. L., Traficante A., et al. 2019, *ApJ*, **886**, 36
- Tan J. C., Beltrán M. T., Caselli P., et al. 2014, *PPVI*, pp 149–172
- Traficante A., Fuller G. A., Peretto N., et al. 2015a, *MNRAS*, **451**, 3089
- Traficante A., Fuller G. A., Pineda J. E., et al. 2015b, *A&A*, **574**, A119
- Traficante A., Fuller G. A., Billot N., et al. 2017, *MNRAS*, **470**, 3882
- Traficante A., Fuller G. A., Smith R. J., et al. 2018a, *MNRAS*, **473**, 4975
- Traficante A., Duarte-Cabral A., Elia D., et al. 2018b, *MNRAS*, **477**, 2220
- Traficante A., Lee Y. N., Hennebelle P., et al. 2018c, *A&A*, **619**, L7
- Urquhart J. S., König C., Giannetti A., et al. 2018, *MNRAS*, **473**, 1059
- Vázquez-Semadeni E., Palau A., Ballesteros-Paredes J., et al. 2019, *MNRAS*, **490**, 3061
- Wang P., Li Z.-Y., Abel T., et al. 2010, *ApJ*, **709**, 27
- Wyrowski F., Güsten R., Menten K. M., et al. 2016, *A&A*, **585**, A149
- Yuan J., Li J.-Z., Wu Y., et al. 2018, *ApJ*, **852**, 12
- Zhang Q., Wang K., Lu X., et al. 2015, *ApJ*, **804**, 141
- Zhang S., Zavagno A., López-Sepulcre A., et al. 2020, arXiv e-prints, p. [arXiv:2012.07738](https://arxiv.org/abs/2012.07738)

APPENDIX A: COMPARISON BETWEEN PHOTOMETRY CODES

In this Appendix we explore the differences between *Hyper* and *astrodendro* applied to our ALMA data.

These codes were designed for different purposes: *Hyper* (Traficante et al. 2015a) was initially written to identify and perform the photometry of dense star-forming regions in the crowded, background-dominated *Herschel* images. *Astrodendro* (Rosolowsky et al. 2008) was designed to compute dendrograms and decompose the images into various hierarchical layers. The main differences of these two approaches can be

separated in the differences in the source identification and in the source photometry.

A1 Source identification

The *Hyper* algorithm uses a finding algorithm which identifies peaks in a high-pass filtered image, and for each peak it performs a 2d-Gaussian fit on the real image. Therefore a "source" is defined as a 2d-Gaussian structure. On the other hand, *astrodendro* performs a dendrogram analysis which identifies leaves and branches in a hierarchical structure based on the emission across the field, with no impositions to the source shape. The smallest leaves are identified as "source" and are not necessarily 2d-Gaussians.

The different extraction algorithms can produce a different number of sources identified in each field, depending on the intensity of the main peaks and on the distribution of the source fluxes, which influence the separation between leaves and trunks (for *astrodendro*).

Astrodendro has three parameters that can be tuned to optimize the source extraction and photometry: *min_value*, the lowest value that can be considered in the map as a potential source; *min_delta*, i.e. the difference between the peak flux and each pixel flux, needed to identify up to which level a leaf independent from another, and when it should be merged in the tree; *min_npix*, the minimum number of pixels needed to consider each identified entity as a single and independent leaf.

After several tests with all our sources, we fixed these parameters to *min_value*=5 times the map *rms* estimated with a sigma-clipping algorithm, *min_delta*= 0.2σ and *min_npix*=2 for the entire sample.

With these numbers we identify 47 sources to be compared with the 55 of the *Hyper* extraction. *Astrodendro* works reasonably well in relatively crowded regions, but with these parameters it fails to identify single fragments in highly confused regions. In Figure A1 we show the sources identified with *Hyper* and *Astrodendro* (also represented with a 2d-Gaussian derived from the *astrodendro* parameters) in the central region of source HIGALBM327.3918+0.1996, where the different fragments that *Hyper* identifies are merged in a single leaf. Although the *astrodendro* parameters can be fine-tuned for each specific source, we did not find a combination of values that allowed us to recover the 5 sources that *Hyper* identified in the central region of HIGALBM327.3918+0.1996.

A2 Source photometry

The main differences in the flux estimation between the two tested algorithms are that *astrodendro* does not account for any background emission, and it is not able to deblend sources that are overlapping along the line of sight. These two conditions, in particular a strong background contribution to the source fluxes, can be critical in our ALMA data. The example of source HIGALBM327.3918+0.1996 in Figure A1 is a good example.

To compare the *astrodendro* and *Hyper* fluxes in a coherent way, we have followed two approaches: first, we have run *Hyper* without subtracting any background, therefore making the *Hyper* fluxes coherent with the *astrodendro* results;

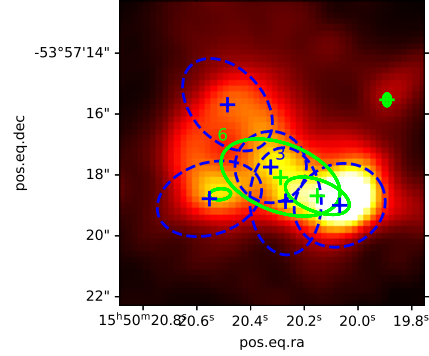


Figure A1. Central region of source HIGALBM327.3918+0.1996 as seen by ALMA at 1.3mm. The blue ellipses are the sources identified by *Hyper*. The green ellipses are those corresponding to the *astrodendro* source identification.

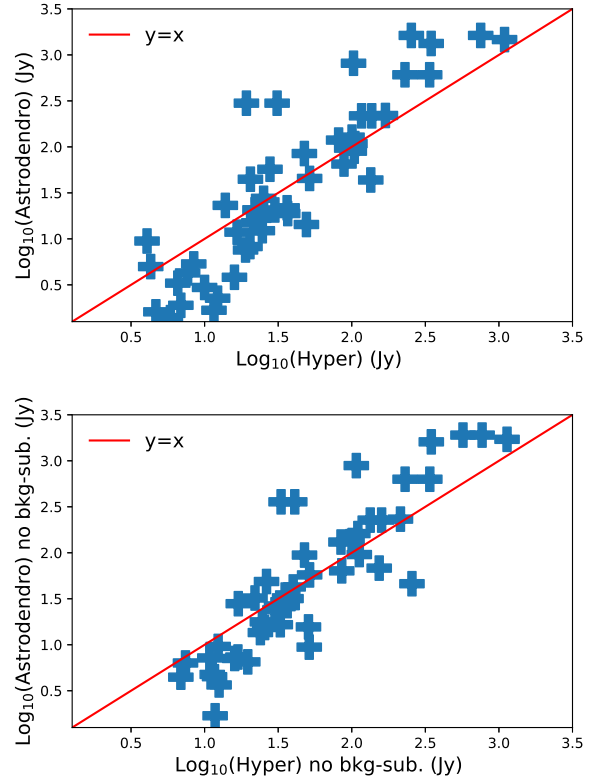


Figure A2. *Upper panel:* *Hyper* fluxes versus *astrodendro* fluxes for the 47 fragments in common. Both fluxes have been background subtracted as explained in the text. *Lower panel:* same plot, but with fluxes integrated without any background subtraction for both *Hyper* and *astrodendro* sources.

then, we have used the *astrodendro* background estimation done with the sigma-clipping approach as a background value to subtract at the whole map, in order to make these fluxes as much coherent as possible with the *Hyper* background-subtracted fluxes.

In Figure A2 we show the comparison of the fluxes of the 47 sources in common with both algorithms in the two cases described. The red-line in both plots is the bisector line. The

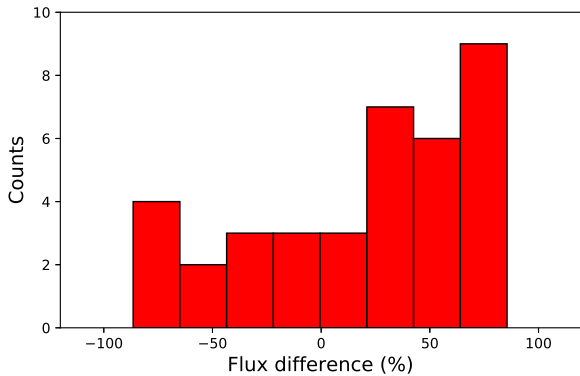


Figure A3. Distribution of fluxes difference (in %) between *Hyper* and astrodenro fluxes for the 37 cases where the fragments are relatively isolated and well identified with both algorithms.

fluxes are statistically in good agreement with correlation coefficients of $\rho = 0.88$ and $\rho = 0.87$ in case of no background subtraction and with background subtraction, respectively. In 10 cases the astrodenro flux is significantly larger than the *Hyper* flux (more than 100% of difference), but these are cases where astrodenro cannot disentangle *Hyper* sources like in Figure A1. In Figure A3 we show the histogram of the flux difference (in %) between the two methods for the remaining 37 sources, excluding the 10 cases just discussed. The absolute average flux differences in this (relatively small) sample is $\simeq 48\%$, and relatively well distributed around the center (the mean value of the distribution is $\simeq 18\%$).

These simple tests show that the main differences between the algorithms may lead to significantly different results on single objects, but these differences may be averaged-out on large samples. At the same time, the fine-tuning for each single source of the astrodenro parameters seems necessary to properly identify ALMA fragments in complex and crowded regions.

We want to stress that there is no reason to prefer one algorithm or another *a-priori*, as long as the results are discussed within the framework of the chosen algorithm which will produce a definition of the ALMA fragments and of their properties (e.g. derived radius, integrated flux) which can be substantially different from one approach to another.

We decided to choose the *Hyper* algorithm to work with a definition of the fragment that is consistent with the definition of the parent clump that we extracted from the original Hi-GAL images.

APPENDIX B: FRAGMENTS PROPERTIES

In this Appendix we report the Table with all the properties of the 55 fragments obtained as described in the main text.

DESIGNATION	ALMA_ID	α	δ	FWHM 1 (")	FWHM 2 (")	PA ($^{\circ}$)	Peak Flux (mJy beam $^{-1}$)	Flux (mJy)	R_f (pc)	M_f (M_{\odot})	Σ_f (g cm $^{-2}$)
HIGALBM327.3918+0.1996	1	15:50:18.2328	-53:57:07.2	1.35	1.52	114.17	56.62	100.414	0.036	44.89	2.32
HIGALBM327.3918+0.1996	2	15:50:18.4344	-53:57:07.056	1.17	1.76	182.4	16.32	31.091	0.036	13.9	0.72
HIGALBM327.3918+0.1996	3	15:50:18.4896	-53:57:05.94	1.17	1.17	254.49	13.09	19.236	0.029	8.6	0.67
HIGALBM327.3918+0.1996	4	15:50:18.7176	-53:57:06.984	1.17	1.76	108.08	20.87	49.191	0.036	21.99	1.13
HIGALBM327.3918+0.1996	5	15:50:20.0832	-53:57:07.668	1.35	1.76	127.21	14.33	25.177	0.039	11.25	0.5
HIGALBM327.3918+0.1996	6	15:50:18.6504	-53:57:03.888	1.17	1.76	222.8	12.31	31.422	0.036	14.04	0.72
HIGALBM327.3918+0.1996	7	15:50:19.2864	-53:57:07.524	1.17	1.62	102.54	15.27	24.684	0.034	11.04	0.62
HIGALBM327.3918+0.1996	8	15:50:19.6296	-53:57:07.488	1.29	1.76	263.43	9.50	20.338	0.038	9.09	0.43
HIGALBM327.3918+0.1996	9	15:50:16.776	-53:57:02.232	1.41	1.76	126.06	10.01	15.952	0.039	7.13	0.31
HIGALBM327.4022+0.4449	1	15:49:19.3248	-53:45:14.256	1.29	1.76	101.74	225.63	338.342	0.034	121.76	7.08
HIGALBM327.4022+0.4449	2	15:49:19.4736	-53:45:14.364	1.17	1.76	97.95	177.66	346.478	0.032	124.69	7.99
HIGALBM327.4022+0.4449	3	15:49:19.2168	-53:45:13.212	1.17	1.76	133.53	127.53	229.981	0.032	82.77	5.3
HIGALBM327.4022+0.4449	4	15:49:19.7112	-53:45:14.58	1.17	1.76	101.18	84.93	134.643	0.032	48.46	3.1
HIGALBM327.4022+0.4449	5	15:49:19.356	-53:45:11.448	1.65	1.76	113.6	40.81	127.368	0.038	45.84	2.08
HIGALBM331.1314-0.2438	1	16:10:59.7408	-51:50:22.812	1.2	1.75	168.77	526.54	751.879	0.035	309.28	17.0
HIGALBM331.1314-0.2438	2	16:10:59.76	-51:50:24.36	1.16	1.56	177.97	178.71	254.008	0.032	104.49	6.66
HIGALBM332.6045-0.1674	1	16:17:29.3256	-50:46:12.612	1.26	1.75	266.6	39.39	81.416	0.022	18.03	2.45
HIGALBM332.6045-0.1674	2	16:17:30.2832	-50:46:11.82	1.17	1.75	251.81	4.85	12.259	0.021	2.71	0.4
HIGALBM338.9260+0.6340	1	16:40:13.9296	-45:38:29.58	1.29	1.62	102.51	82.15	169.367	0.029	68.87	5.39
HIGALBM338.9260+0.6340	2	16:40:14.256	-45:38:30.696	1.2	1.37	115.84	65.69	104.051	0.026	42.31	4.21
HIGALBM338.9260+0.6340	3	16:40:13.5648	-45:38:33.216	1.32	1.62	140.9	47.40	105.084	0.029	42.73	3.27
HIGALBM338.9260+0.6340	4	16:40:12.9384	-45:38:26.592	1.08	1.62	143.47	15.80	23.299	0.027	9.48	0.89
HIGALBM341.2149-0.2359	1	16:52:23.736	-44:27:55.008	1.07	1.6	146.02	22.89	47.639	0.022	9.52	1.32
HIGALBM341.2149-0.2359	2	16:52:22.3608	-44:28:02.532	1.28	1.6	166.54	21.92	51.711	0.024	10.33	1.2
HIGALBM341.2149-0.2359	3	16:52:23.6784	-44:27:53.964	1.07	1.6	146.8	14.33	20.481	0.022	4.09	0.57
HIGALBM341.2149-0.2359	4	16:52:23.9232	-44:27:56.232	1.07	1.07	137.16	15.27	21.614	0.018	4.32	0.9
HIGALBM341.2149-0.2359	5	16:52:24.0672	-44:27:54.54	1.07	1.07	235.1	11.91	16.619	0.018	3.32	0.69
HIGALBM341.2149-0.2359	6	16:52:22.4136	-44:27:43.776	1.07	1.07	180.0	2.91	4.062	0.018	0.81	0.17
HIGALBM341.2149-0.2359	7	16:52:22.0656	-44:27:55.08	1.07	1.6	117.85	6.81	11.578	0.022	2.32	0.32
HIGALBM343.5212-0.5172	1	17:01:34.0104	-42:50:20.04	1.32	1.6	257.92	8.11	13.828	0.021	2.13	0.31
HIGALBM343.5212-0.5172	2	17:01:33.7872	-42:50:19.428	1.07	1.11	129.75	3.08	5.852	0.016	0.9	0.23
HIGALBM343.5212-0.5172	3	17:01:33.5736	-42:50:10.104	1.28	1.54	230.77	3.08	4.666	0.021	0.71	0.11
HIGALBM343.5212-0.5172	4	17:01:33.8304	-42:50:21.3	1.39	1.6	131.13	1.47	4.928	0.022	0.75	0.1
HIGALBM343.5212-0.5172	5	17:01:33.7848	-42:50:17.736	1.07	1.07	229.02	3.69	4.695	0.016	0.72	0.19
HIGALBM343.7560-0.1629	1	17:00:49.8792	-42:26:09.096	1.19	1.37	137.15	708.58	1092.309	0.012	73.35	31.81
HIGALBM344.1032-0.6609	1	17:04:06.6864	-42:27:57.852	1.37	1.6	134.08	17.18	36.354	0.014	2.44	0.79
HIGALBM344.1032-0.6609	2	17:04:07.5072	-42:28:02.82	1.11	1.59	101.01	6.48	9.997	0.013	0.67	0.27
HIGALBM344.1032-0.6609	3	17:04:06.972	-42:28:06.708	1.22	1.6	143.01	4.04	6.317	0.014	0.42	0.15

Table B1. Properties of the 55 fragments identified in our 13 massive clumps. *col.1*: Clump designation; *col.2*: ALMA ID following the *Hyper* identification number in each clump; *col.3-4*: coordinates of the fragments peak position; *cols. 5-7*: FWHMs and position angles of the 2d-Gaussian fit used to estimate the source integrated flux; *col.8*: peak flux (background subtracted); *col.9*: integrated flux within the ellipse defined by the 2 FWHMs and the PA; *col.10-12*: radius, mass and surface density of each fragment derived as described in the text.

DESIGNATION	ALMA_ID	α	δ	FWHM 1 (")	FWHM 2 (")	PA ($^{\circ}$)	Peak Flux (mJy beam $^{-1}$)	Flux (mJy)	R_f (pc)	M_f (M_{\odot})	Σ_f (g cm $^{-2}$)
HIGALBM344.2210-0.5932	1	17:04:12.936	-42:19:52.14	1.07	1.6	112.52	66.03	136.753	0.013	9.18	3.79
HIGALBM344.2210-0.5932	2	17:04:12.6048	-42:19:54.192	1.18	1.6	253.73	39.46	88.574	0.013	5.95	2.23
HIGALBM344.2210-0.5932	3	17:04:12.8184	-42:19:52.716	1.07	1.6	222.54	44.18	116.642	0.013	7.83	3.24
HIGALBM344.2210-0.5932	4	17:04:12.7728	-42:19:54.624	1.07	1.6	171.74	38.88	102.784	0.013	6.9	2.85
HIGALBM344.2210-0.5932	5	17:04:12.9672	-42:19:57.36	1.33	1.59	163.19	20.95	27.813	0.014	1.87	0.63
HIGALBM344.2210-0.5932	6	17:04:12.3504	-42:19:46.884	1.07	1.6	145.7	16.23	36.709	0.013	2.47	1.02
HIGALBM344.2210-0.5932	7	17:04:12.636	-42:19:49.08	1.6	1.6	172.08	6.62	18.98	0.016	1.27	0.35
HIGALBM24.0116+0.4897	1	18:33:18.2952	-7:42:26.136	1.38	2.01	237.29	14.87	30.044	0.042	31.86	1.19
HIGALBM24.0116+0.4897	2	18:33:18.516	-7:42:25.74	1.34	2.01	103.04	6.04	8.438	0.042	8.95	0.34
HIGALBM28.1957-0.0724	1	18:43:02.8344	-4:14:50.784	1.58	2.03	241.43	3.13	4.302	0.047	4.81	0.15
HIGALBM28.1957-0.0724	2	18:43:03.2592	-4:15:08.892	1.39	1.39	180.0	4.17	6.571	0.036	7.35	0.37
HIGALBM28.1957-0.0724	3	18:43:01.9992	-4:14:48.084	1.39	2.09	92.84	3.51	6.897	0.044	7.71	0.26
HIGALBM28.1957-0.0724	4	18:43:02.5104	-4:14:51.072	1.41	2.09	121.0	1.37	2.292	0.045	2.57	0.09
HIGALBM31.9462+0.0759	1	18:49:22.104	-0:50:32.352	1.55	1.94	95.71	12.32	21.993	0.046	25.9	0.81
HIGALBM31.9462+0.0759	2	18:49:22.1448	-0:50:45.708	1.61	2.11	227.25	4.35	7.667	0.049	9.03	0.25
HIGALBM31.9462+0.0759	3	18:49:22.08	-0:50:34.98	1.41	2.11	182.88	1.95	2.758	0.046	3.25	0.1
HIGALBM31.9462+0.0759	4	18:49:22.3104	-0:50:31.56	1.41	1.59	231.19	1.62	2.217	0.04	2.61	0.11

APPENDIX C: HEATMAP OF PEARSON'S COEFFICIENTS

In this Appendix we show the correlation matrix, or heatmap for all the pairs of parameters discussed in the main text. It includes parameters of the clumps: mass M_{cl} , L/M ratio L_{cl}/M_{cl} , surface density Σ_{cl} , mass accretion rate \dot{M}_{cl} and virial parameter $\alpha_{vir,cl}$; parameters of the fragments: the number of fragments in each clump $\#_f$, the minimum 2D (3D) distances between fragments, $d_{min,2D}$ ($d_{min,3D}$), the total mass of fragments in each clump M_f , the mass and surface density of the most massive and of the densest fragment in each clump, $M_{f,max}$ and $\Sigma_{f,max}$, respectively; parameters that combine clumps and fragments properties: the instantaneous clump formation efficiency (CFE), i.e. the ratio between the total mass of the fragments in each clump and the mass of the clump (e.g. Anderson et al. 2021), and the ratio between the clump 2D Jeans length (3D corrected) and the minimum distance between fragments in each clump, $\lambda_{Jr,2D}$ ($\lambda_{Jr,3D}$).

APPENDIX D: TEMPERATURE UNCERTAINTIES

In this Appendix we describe how the uncertainties in the dust temperatures of our fragments may impact our results. To investigate the impact on the temperature uncertainties, we have re-evaluated the temperature-dependent properties of our fragments described in Section 5.2 using a different set of temperatures for each fragment. Namely, we have run a set of 100 Monte Carlo simulations and in each realization we have assigned to the fragments a random dust temperature T_{lim} within the boundaries described in Table 4. For each run we have re-evaluated the scatter-plots in Figures 7, 8, 9 and 10 and the Pearson's correlation coefficients. In Figure D1 there is an example of one of this realization for each of the 4 scatter-plots, compared with the reference values assumed in the main text (using $T = T_f$), and in Table D there are the mean, minimum and maximum values of the Pearson's coefficients for the 100 runs and for the reference values assumed in the main text using $T = T_f$. We also show the different slopes of the linear fit (in log-log space) to the $\alpha_{vir,cl}$ versus M_f relation for the 100 realizations. Although the mass estimation can significantly vary for each single fragment (see Section 3.2.2), the statistical (anti)correlations are preserved in all runs (as well as the negative slope in the fit of the $\alpha_{vir,cl}$ versus M_f distribution), which assures that our conclusions are robust against the temperature uncertainties.

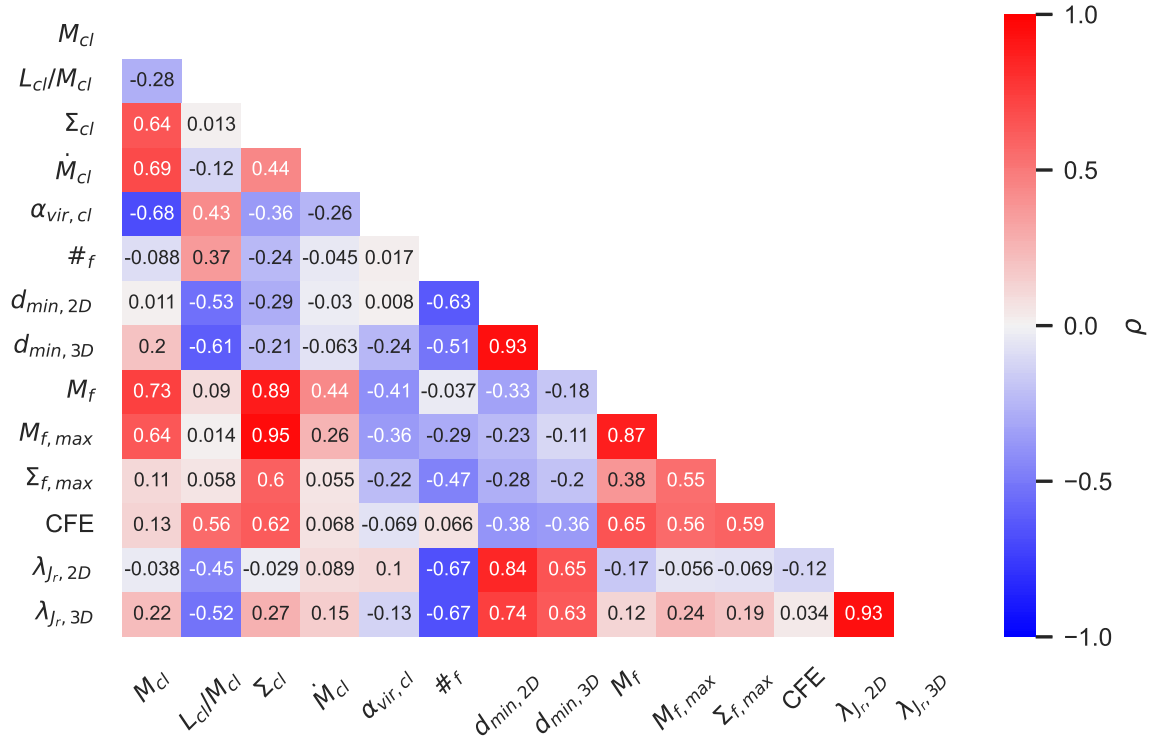


Figure C1. Heatmap of the Pearson's correlation coefficients ρ between several properties derived for clumps and fragments, as described in the text. The heatmap is colour-coded such that the bluest cells represents the highest degree of anti-correlation (approaching $\rho = -1$), and the reddest cells the highest degree of correlation (approaching $\rho = 1$). The value of ρ for each given pair of parameters is reported within each cell.

ρ_{val}	M_f vs. M_{cl}	$\Sigma_{f,max}$ vs. Σ_{cl}	M_f vs. \dot{M}_{cl}	$\alpha_{vir,cl}$ vs. M_f	Slope ($\alpha_{vir,cl}$ vs. M_f)
MEAN	0.72	0.61	0.48	-0.40	-0.24
MIN	0.63	0.32	0.21	-0.48	-0.33
MAX	0.86	0.90	0.81	-0.33	-0.17
REF	0.73	0.60	0.44	-0.41	-0.29

Table D1. Distribution of the Pearson's correlation coefficients for the temperature dependent parameters described in Section 5.2 for the 100 simulations. *Col. 1:* mean, min, max and reference value of the Pearson's coefficients (ρ_{val}); *Cols. 2-5:* (ρ_{val}) for M_f vs. M_{cl} , $\Sigma_{f,max}$ vs. Σ_{cl} , M_f vs. \dot{M}_{cl} and $\alpha_{vir,cl}$ vs. M_f relations respectively; *Col. 6:* slopes of the linear fit in the log-log space at the $\alpha_{vir,cl}$ vs. M_f distribution.

APPENDIX E: PEARSON'S PARAMETERS

In this Appendix we report the values of the Pearson's correlation coefficients for each pair of parameter considered in the heatmap in Appendix C. The Table includes the p-val percentiles and confidence intervals at 95% level of confidence assuming uncertainties of each parameter equal to 20% of its value.

This paper has been typeset from a T_EX/L^AT_EX file prepared by the author.

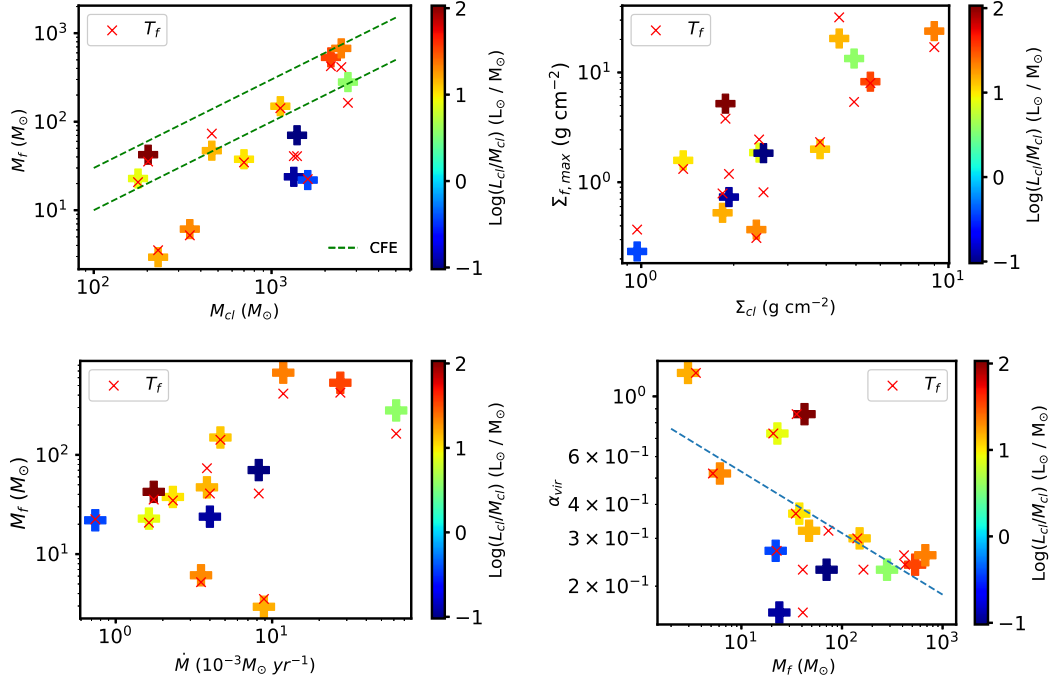


Figure D1. Same distributions of Figures 7, 8, 9 and 10 but for a different realization of the dust temperature of each fragment (and therefore a different estimation of the temperature-dependent parameters). The red crosses are the reference values assumed in the main text assuming $T = T_f$.

Param_1	Param_2	ρ	p-val	CI 95%	Param_1	Param_2	ρ	p-val	CI 95%
M_{cl}	M_{cl}	1.0	0.000	[1.0, 1.0]	$\alpha_{vir,cl}$	M_{cl}	-0.684	0.010	[-0.9, -0.21]
M_{cl}	L_{cl}/M_{cl}	-0.279	0.356	[-0.72, 0.32]	$\alpha_{vir,cl}$	L_{cl}/M_{cl}	0.425	0.147	[-0.16, 0.79]
M_{cl}	Σ_{cl}	0.643	0.018	[0.14, 0.88]	$\alpha_{vir,cl}$	Σ_{cl}	-0.36	0.227	[-0.76, 0.24]
M_{cl}	\dot{M}_{cl}	0.691	0.009	[0.23, 0.9]	$\alpha_{vir,cl}$	\dot{M}_{cl}	-0.257	0.398	[-0.71, 0.34]
M_{cl}	$\alpha_{vir,cl}$	-0.684	0.010	[-0.9, -0.21]	$\alpha_{vir,cl}$	$\alpha_{vir,cl}$	1.0	0.000	[1.0, 1.0]
M_{cl}	$\#_f$	-0.088	0.776	[-0.61, 0.49]	$\alpha_{vir,cl}$	$\#_f$	0.017	0.956	[-0.54, 0.56]
M_{cl}	$d_{min,2D}$	0.011	0.972	[-0.57, 0.58]	$\alpha_{vir,cl}$	$d_{min,2D}$	0.008	0.980	[-0.57, 0.58]
M_{cl}	$d_{min,3D}$	0.202	0.528	[-0.42, 0.7]	$\alpha_{vir,cl}$	$d_{min,3D}$	-0.243	0.446	[-0.72, 0.38]
M_{cl}	M_f	0.728	0.005	[0.29, 0.91]	$\alpha_{vir,cl}$	M_f	-0.407	0.168	[-0.78, 0.19]
M_{cl}	$M_{f,max}$	0.64	0.018	[0.14, 0.88]	$\alpha_{vir,cl}$	$M_{f,max}$	-0.363	0.223	[-0.76, 0.24]
M_{cl}	$\Sigma_{f,max}$	0.106	0.730	[-0.47, 0.62]	$\alpha_{vir,cl}$	$\Sigma_{f,max}$	-0.222	0.465	[-0.69, 0.37]
M_{cl}	CFE	0.13	0.673	[-0.45, 0.64]	$\alpha_{vir,cl}$	CFE	-0.069	0.824	[-0.6, 0.5]
M_{cl}	$\lambda_{J_r,2D}$	-0.038	0.906	[-0.6, 0.55]	$\alpha_{vir,cl}$	$\lambda_{J_r,2D}$	0.104	0.748	[-0.5, 0.64]
M_{cl}	$\lambda_{J_r,3D}$	0.22	0.492	[-0.41, 0.7]	$\alpha_{vir,cl}$	$\lambda_{J_r,3D}$	-0.132	0.683	[-0.66, 0.48]
L_{cl}/M_{cl}	M_{cl}	-0.279	0.356	[-0.72, 0.32]	$\#_f$	M_{cl}	-0.088	0.776	[-0.61, 0.49]
L_{cl}/M_{cl}	L_{cl}/M_{cl}	1.0	0.000	[1.0, 1.0]	$\#_f$	L_{cl}/M_{cl}	0.367	0.218	[-0.23, 0.76]
L_{cl}/M_{cl}	Σ_{cl}	0.013	0.966	[-0.54, 0.56]	$\#_f$	Σ_{cl}	-0.238	0.434	[-0.7, 0.36]
L_{cl}/M_{cl}	\dot{M}_{cl}	-0.125	0.685	[-0.63, 0.46]	$\#_f$	\dot{M}_{cl}	-0.045	0.885	[-0.58, 0.52]
L_{cl}/M_{cl}	$\alpha_{vir,cl}$	0.425	0.147	[-0.16, 0.79]	$\#_f$	$\alpha_{vir,cl}$	0.017	0.956	[-0.54, 0.56]
L_{cl}/M_{cl}	$\#_f$	0.367	0.218	[-0.23, 0.76]	$\#_f$	$\#_f$	1.0	0.000	[1.0, 1.0]
L_{cl}/M_{cl}	$d_{min,2D}$	-0.533	0.074	[-0.85, 0.06]	$\#_f$	$d_{min,2D}$	-0.626	0.029	[-0.88, -0.08]
L_{cl}/M_{cl}	$d_{min,3D}$	-0.615	0.033	[-0.88, -0.06]	$\#_f$	$d_{min,3D}$	-0.51	0.090	[-0.84, 0.09]
L_{cl}/M_{cl}	M_f	0.09	0.769	[-0.48, 0.61]	$\#_f$	M_f	-0.037	0.904	[-0.58, 0.52]
L_{cl}/M_{cl}	$M_{f,max}$	0.014	0.964	[-0.54, 0.56]	$\#_f$	$M_{f,max}$	-0.295	0.328	[-0.73, 0.31]
L_{cl}/M_{cl}	$\Sigma_{f,max}$	0.058	0.851	[-0.51, 0.59]	$\#_f$	$\Sigma_{f,max}$	-0.468	0.107	[-0.81, 0.11]
L_{cl}/M_{cl}	CFE	0.56	0.046	[0.01, 0.85]	$\#_f$	CFE	0.066	0.830	[-0.5, 0.6]
L_{cl}/M_{cl}	$\lambda_{J_r,2D}$	-0.446	0.146	[-0.81, 0.17]	$\#_f$	$\lambda_{J_r,2D}$	-0.668	0.018	[-0.9, -0.15]
L_{cl}/M_{cl}	$\lambda_{J_r,3D}$	-0.519	0.084	[-0.84, 0.08]	$\#_f$	$\lambda_{J_r,3D}$	-0.668	0.018	[-0.9, -0.15]
Σ_{cl}	M_{cl}	0.643	0.018	[0.14, 0.88]	$d_{min,2D}$	M_{cl}	0.011	0.972	[-0.57, 0.58]
Σ_{cl}	L_{cl}/M_{cl}	0.013	0.966	[-0.54, 0.56]	$d_{min,2D}$	L_{cl}/M_{cl}	-0.533	0.074	[-0.85, 0.06]
Σ_{cl}	Σ_{cl}	1.0	0.000	[1.0, 1.0]	$d_{min,2D}$	Σ_{cl}	-0.288	0.363	[-0.74, 0.34]
Σ_{cl}	\dot{M}_{cl}	0.438	0.135	[-0.15, 0.8]	$d_{min,2D}$	\dot{M}_{cl}	-0.03	0.927	[-0.59, 0.55]
Σ_{cl}	$\alpha_{vir,cl}$	-0.36	0.227	[-0.76, 0.24]	$d_{min,2D}$	$\alpha_{vir,cl}$	0.008	0.980	[-0.57, 0.58]
Σ_{cl}	$\#_f$	-0.238	0.434	[-0.7, 0.36]	$d_{min,2D}$	$\#_f$	-0.626	0.029	[-0.88, -0.08]
Σ_{cl}	$d_{min,2D}$	-0.288	0.363	[-0.74, 0.34]	$d_{min,2D}$	$d_{min,2D}$	1.0	0.000	[1.0, 1.0]
Σ_{cl}	$d_{min,3D}$	-0.213	0.507	[-0.7, 0.41]	$d_{min,2D}$	$d_{min,3D}$	0.933	0.000	[0.77, 0.98]
Σ_{cl}	M_f	0.887	0.000	[0.66, 0.97]	$d_{min,2D}$	M_f	-0.331	0.293	[-0.76, 0.3]
Σ_{cl}	$M_{f,max}$	0.946	0.000	[0.82, 0.98]	$d_{min,2D}$	$M_{f,max}$	-0.23	0.472	[-0.71, 0.4]
Σ_{cl}	$\Sigma_{f,max}$	0.6	0.030	[0.07, 0.87]	$d_{min,2D}$	$\Sigma_{f,max}$	-0.278	0.383	[-0.73, 0.35]
Σ_{cl}	CFE	0.62	0.024	[0.11, 0.87]	$d_{min,2D}$	CFE	-0.384	0.217	[-0.79, 0.24]
Σ_{cl}	$\lambda_{J_r,2D}$	-0.029	0.929	[-0.59, 0.55]	$d_{min,2D}$	$\lambda_{J_r,2D}$	0.837	0.001	[0.51, 0.95]
Σ_{cl}	$\lambda_{J_r,3D}$	0.267	0.401	[-0.36, 0.73]	$d_{min,2D}$	$\lambda_{J_r,3D}$	0.735	0.006	[0.28, 0.92]
\dot{M}_{cl}	M_{cl}	0.691	0.009	[0.23, 0.9]	$d_{min,3D}$	M_{cl}	0.202	0.528	[-0.42, 0.7]
\dot{M}_{cl}	L_{cl}/M_{cl}	-0.125	0.685	[-0.63, 0.46]	$d_{min,3D}$	L_{cl}/M_{cl}	-0.615	0.033	[-0.88, -0.06]
\dot{M}_{cl}	Σ_{cl}	0.438	0.135	[-0.15, 0.8]	$d_{min,3D}$	Σ_{cl}	-0.213	0.507	[-0.7, 0.41]
\dot{M}_{cl}	\dot{M}_{cl}	1.0	0.000	[1.0, 1.0]	$d_{min,3D}$	\dot{M}_{cl}	-0.063	0.845	[-0.61, 0.53]
\dot{M}_{cl}	$\alpha_{vir,cl}$	-0.257	0.398	[-0.71, 0.34]	$d_{min,3D}$	$\alpha_{vir,cl}$	-0.243	0.446	[-0.72, 0.38]
\dot{M}_{cl}	$\#_f$	-0.045	0.885	[-0.58, 0.52]	$d_{min,3D}$	$\#_f$	-0.51	0.090	[-0.84, 0.09]
\dot{M}_{cl}	$d_{min,2D}$	-0.03	0.927	[-0.59, 0.55]	$d_{min,3D}$	$d_{min,2D}$	0.933	0.000	[0.77, 0.98]
\dot{M}_{cl}	$d_{min,3D}$	-0.063	0.845	[-0.61, 0.53]	$d_{min,3D}$	$d_{min,3D}$	1.0	0.000	[1.0, 1.0]
\dot{M}_{cl}	M_f	0.436	0.136	[-0.15, 0.8]	$d_{min,3D}$	M_f	-0.185	0.566	[-0.69, 0.44]
\dot{M}_{cl}	$M_{f,max}$	0.256	0.398	[-0.34, 0.71]	$d_{min,3D}$	$M_{f,max}$	-0.113	0.726	[-0.65, 0.49]
\dot{M}_{cl}	$\Sigma_{f,max}$	0.055	0.858	[-0.51, 0.59]	$d_{min,3D}$	$\Sigma_{f,max}$	-0.202	0.528	[-0.7, 0.42]
\dot{M}_{cl}	CFE	0.068	0.825	[-0.5, 0.6]	$d_{min,3D}$	CFE	-0.362	0.248	[-0.77, 0.27]
\dot{M}_{cl}	$\lambda_{J_r,2D}$	0.089	0.784	[-0.51, 0.63]	$d_{min,3D}$	$\lambda_{J_r,2D}$	0.651	0.022	[0.12, 0.89]
\dot{M}_{cl}	$\lambda_{J_r,3D}$	0.15	0.641	[-0.46, 0.67]	$d_{min,3D}$	$\lambda_{J_r,3D}$	0.631	0.028	[0.09, 0.88]

Table E1. Pearson's coefficients and statistical values for each pair of parameters described in the heatmap in Appendix C. *Cols 1-2:* pair of parameter considered; *Col3* value of the Pearson's correlation coefficient for the given pair of parameters; *Cols 4-5* p-value percentiles and confidence interval at 95% for the given pair of parameters.

Param_1	Param_2	ρ	p-val	CI 95%
M_f	M_{cl}	0.728	0.005	[0.29, 0.91]
M_f	L_{cl}/M_{cl}	0.09	0.769	[-0.48, 0.61]
M_f	Σ_{cl}	0.887	0.000	[0.66, 0.97]
M_f	\dot{M}_{cl}	0.436	0.136	[-0.15, 0.8]
M_f	$\alpha_{vir,cl}$	-0.407	0.168	[-0.78, 0.19]
M_f	$\#_f$	-0.037	0.904	[-0.58, 0.52]
M_f	$d_{min,2D}$	-0.331	0.293	[-0.76, 0.3]
M_f	$d_{min,3D}$	-0.185	0.566	[-0.69, 0.44]
M_f	M_f	1.0	0.000	[1.0, 1.0]
M_f	$M_{f,max}$	0.87	0.000	[0.61, 0.96]
M_f	$\Sigma_{f,max}$	0.381	0.199	[-0.21, 0.77]
M_f	CFE	0.65	0.016	[0.15, 0.88]
M_f	$\lambda_{J_r,2D}$	-0.173	0.590	[-0.68, 0.44]
M_f	$\lambda_{J_r,3D}$	0.123	0.704	[-0.49, 0.65]
$M_{f,max}$	M_{cl}	0.64	0.018	[0.14, 0.88]
$M_{f,max}$	L_{cl}/M_{cl}	0.014	0.964	[-0.54, 0.56]
$M_{f,max}$	Σ_{cl}	0.946	0.000	[0.82, 0.98]
$M_{f,max}$	\dot{M}_{cl}	0.256	0.398	[-0.34, 0.71]
$M_{f,max}$	$\alpha_{vir,cl}$	-0.363	0.223	[-0.76, 0.24]
$M_{f,max}$	$\#_f$	-0.295	0.328	[-0.73, 0.31]
$M_{f,max}$	$d_{min,2D}$	-0.23	0.472	[-0.71, 0.4]
$M_{f,max}$	$d_{min,3D}$	-0.113	0.726	[-0.65, 0.49]
$M_{f,max}$	M_f	0.87	0.000	[0.61, 0.96]
$M_{f,max}$	$M_{f,max}$	1.0	0.000	[1.0, 1.0]
$M_{f,max}$	$\Sigma_{f,max}$	0.546	0.054	[-0.01, 0.84]
$M_{f,max}$	CFE	0.558	0.047	[0.01, 0.85]
$M_{f,max}$	$\lambda_{J_r,2D}$	-0.056	0.862	[-0.61, 0.53]
$M_{f,max}$	$\lambda_{J_r,3D}$	0.242	0.449	[-0.39, 0.72]
$\Sigma_{f,max}$	M_{cl}	0.106	0.730	[-0.47, 0.62]
$\Sigma_{f,max}$	L_{cl}/M_{cl}	0.058	0.851	[-0.51, 0.59]
$\Sigma_{f,max}$	Σ_{cl}	0.6	0.030	[0.07, 0.87]
$\Sigma_{f,max}$	\dot{M}_{cl}	0.055	0.858	[-0.51, 0.59]
$\Sigma_{f,max}$	$\alpha_{vir,cl}$	-0.222	0.465	[-0.69, 0.37]
$\Sigma_{f,max}$	$\#_f$	-0.468	0.107	[-0.81, 0.11]
$\Sigma_{f,max}$	$d_{min,2D}$	-0.278	0.383	[-0.73, 0.35]
$\Sigma_{f,max}$	$d_{min,3D}$	-0.202	0.528	[-0.7, 0.42]
$\Sigma_{f,max}$	M_f	0.381	0.199	[-0.21, 0.77]
$\Sigma_{f,max}$	$M_{f,max}$	0.546	0.054	[-0.01, 0.84]
$\Sigma_{f,max}$	$\Sigma_{f,max}$	1.0	0.000	[1.0, 1.0]
$\Sigma_{f,max}$	CFE	0.592	0.033	[0.06, 0.86]
$\Sigma_{f,max}$	$\lambda_{J_r,2D}$	-0.069	0.831	[-0.62, 0.53]
$\Sigma_{f,max}$	$\lambda_{J_r,3D}$	0.189	0.555	[-0.43, 0.69]
CFE	M_{cl}	0.13	0.673	[-0.45, 0.64]
CFE	L_{cl}/M_{cl}	0.56	0.046	[0.01, 0.85]
CFE	Σ_{cl}	0.62	0.024	[0.11, 0.87]
CFE	\dot{M}_{cl}	0.068	0.825	[-0.5, 0.6]
CFE	$\alpha_{vir,cl}$	-0.069	0.824	[-0.6, 0.5]
CFE	$\#_f$	0.066	0.830	[-0.5, 0.6]
CFE	$d_{min,2D}$	-0.384	0.217	[-0.79, 0.24]
CFE	$d_{min,3D}$	-0.362	0.248	[-0.77, 0.27]
CFE	M_f	0.65	0.016	[0.15, 0.88]
CFE	$M_{f,max}$	0.558	0.047	[0.01, 0.85]
CFE	$\Sigma_{f,max}$	0.592	0.033	[0.06, 0.86]
CFE	CFE	1.0	0.000	[1.0, 1.0]
CFE	$\lambda_{J_r,2D}$	-0.124	0.700	[-0.65, 0.48]
CFE	$\lambda_{J_r,3D}$	0.034	0.915	[-0.55, 0.6]

Param_1	Param_2	ρ	p-val	CI 95%
$\lambda_{J_r,2D}$	M_{cl}	-0.038	0.906	[-0.6, 0.55]
$\lambda_{J_r,2D}$	L_{cl}/M_{cl}	-0.446	0.146	[-0.81, 0.17]
$\lambda_{J_r,2D}$	Σ_{cl}	-0.029	0.929	[-0.59, 0.55]
$\lambda_{J_r,2D}$	\dot{M}_{cl}	0.089	0.784	[-0.51, 0.63]
$\lambda_{J_r,2D}$	$\alpha_{vir,cl}$	0.104	0.748	[-0.5, 0.64]
$\lambda_{J_r,2D}$	$\#_f$	-0.668	0.018	[-0.9, -0.15]
$\lambda_{J_r,2D}$	$d_{min,2D}$	0.837	0.001	[0.51, 0.95]
$\lambda_{J_r,2D}$	$d_{min,3D}$	0.651	0.022	[0.12, 0.89]
$\lambda_{J_r,2D}$	M_f	-0.173	0.590	[-0.68, 0.44]
$\lambda_{J_r,2D}$	$M_{f,max}$	-0.056	0.862	[-0.61, 0.53]
$\lambda_{J_r,2D}$	$\Sigma_{f,max}$	-0.069	0.831	[-0.62, 0.53]
$\lambda_{J_r,2D}$	CFE	-0.124	0.700	[-0.65, 0.48]
$\lambda_{J_r,2D}$	$\lambda_{J_r,2D}$	1.0	0.000	[1.0, 1.0]
$\lambda_{J_r,3D}$	$\lambda_{J_r,3D}$	0.933	0.000	[0.77, 0.98]
$\lambda_{J_r,3D}$	M_{cl}	0.22	0.492	[-0.41, 0.7]
$\lambda_{J_r,3D}$	L_{cl}/M_{cl}	-0.519	0.084	[-0.84, 0.08]
$\lambda_{J_r,3D}$	Σ_{cl}	0.267	0.401	[-0.36, 0.73]
$\lambda_{J_r,3D}$	\dot{M}_{cl}	0.15	0.641	[-0.46, 0.67]
$\lambda_{J_r,3D}$	$\alpha_{vir,cl}$	-0.132	0.683	[-0.66, 0.48]
$\lambda_{J_r,3D}$	$\#_f$	-0.668	0.018	[-0.9, -0.15]
$\lambda_{J_r,3D}$	$d_{min,2D}$	0.735	0.006	[0.28, 0.92]
$\lambda_{J_r,3D}$	$d_{min,3D}$	0.631	0.028	[0.09, 0.88]
$\lambda_{J_r,3D}$	M_f	0.123	0.704	[-0.49, 0.65]
$\lambda_{J_r,3D}$	$M_{f,max}$	0.242	0.449	[-0.39, 0.72]
$\lambda_{J_r,3D}$	$\Sigma_{f,max}$	0.189	0.555	[-0.43, 0.69]
$\lambda_{J_r,3D}$	CFE	0.034	0.915	[-0.55, 0.6]
$\lambda_{J_r,3D}$	$\lambda_{J_r,2D}$	0.933	0.000	[0.77, 0.98]
$\lambda_{J_r,3D}$	$\lambda_{J_r,3D}$	1.0	0.000	[1.0, 1.0]